

# **1 Interferometric synthetic aperture radar–GPS 2 integration: Interseismic train accumulation across the Hunter 3 Mountain fault in the eastern California shear zone**

4 Noel Gourmelen,<sup>1</sup> Falk Amelung,<sup>1,2</sup> and Riccardo Lanari<sup>3</sup>

5 Received 20 October 2009; revised 24 April 2010; accepted 4 May 2010; published XX Month 2010.

[1] The principal limitations of interferometric synthetic aperture radar (InSAR) to measure subtle, long-wavelength deformation are uncertainties associated with the satellite orbits. We propose a method to remove orbital phase errors from the InSAR data by integrating InSAR and continuous GPS time series. We model the along-track variation of the baseline errors as second-order polynomials and estimate the coefficients using the continuous GPS measurements. We apply this method to a 600 km long region encompassing the Basin and Range and the eastern California shear zone. Comparison of the corrected InSAR velocities with independent GPS data shows that this method removes the long-wavelength InSAR errors. The InSAR data reveal a region of sharp variation in the line-of-sight velocity across the Hunter Mountain fault. We model the deformation as interseismic elastic strain accumulation across a strike-slip fault. The modeling suggests a fault slip rate of  $4.9 \pm 0.8$  mm/yr and a locking depth of  $2 \pm 0.4$  km. The shallow locking depth suggests that the Hunter Mountain fault is a transfer fault between low angle normal faults in the area.

**20 Citation:** Gourmelen, N., F. Amelung, and R. Lanari (2010), Interferometric synthetic aperture radar–GPS integration:  
21 Interseismic train accumulation across the Hunter Mountain fault in the eastern California shear zone, *J. Geophys. Res.*, 115,  
22 XXXXXX, doi:10.1029/2009JB007064.

23 1. Introduction

[2] Interferometric synthetic aperture radar (InSAR) has been used successfully to measure and study surface deformation due to several phenomena such as glacier movements [Goldstein *et al.*, 1993], earthquakes [Massonnet *et al.*, 1994], and volcano inflation [Amelung *et al.*, 2000]. The measurement of subtle, long-wavelength deformation (>50 km), such as interseismic and postseismic deformation [Massonnet, 1997; Pollitz *et al.*, 2000], remains a challenge. The precision of the InSAR measurement is affected by decorrelation phenomena, phase contributions due to atmospheric water vapor and ionospheric effects, and uncertainties in the position of the satellites. The uncertainties in the position of the satellites (orbital errors) degrade the precision of the measurements from millimeters (the instrumental precision) to centimeters or more for long-wavelength deformation; the orbital errors cause relative line-of-sight (LOS) displacements over tens to hundreds of kilometers in the interferograms (referred to in this paper as orbital phase errors) that are difficult to separate from LOS displacements caused

by interseismic strain accumulation. Precise orbits, such as the ones provided by the Delft Institute for Earth-Oriented Space Research (DEOS), have a standard deviation on the order of 15 cm [Scharroo, 2002], which translate into several centimeters of LOS displacements.

[3] Since the end of the 1990s, techniques for the simultaneous analysis of large numbers of SAR acquisitions (there are more than 150 acquisitions for most of Europe and 50–100 acquisition for other parts of the worlds) have led to time-dependent measurements [Ferretti *et al.*, 2001; Berardino *et al.*, 2002; Lanari *et al.*, 2004; Hooper *et al.*, 2004; Casu *et al.*, 2008]. These time series techniques, often referred to as persistent scatterers (PS) and small baseline subset (SBAS) approaches, have significantly improved measurement precision. In these algorithms, only those pixels remaining coherent in all or part of the interferograms are exploited; they are detected (and subsequently analyzed) by carrying statistical [Ferretti *et al.*, 2005] or coherence [Berardino *et al.*, 2002] analyses on a large SAR data set. The atmospheric phase contributions or atmospheric phase screen (APS) can be extracted and removed by applying spatial-temporal filtering on the time series [Ferretti *et al.*, 2001; Berardino *et al.*, 2002].

[4] Large-scale tectonic processes, such as interseismic deformation across entire fault zones and postseismic deformation following large earthquakes, can be studied using multiple, consecutive radar frames [Peltzer *et al.*, 2001; Wright *et al.*, 2004; Fialko, 2006; Biggs *et al.*, 2005; Cvetkovic *et al.*, 2004; Berardino *et al.*, 2002].

<sup>1</sup>School of Marine and Atmospheric Science, University of Miami, Miami, Florida, USA.

<sup>2</sup>Now at School of Earth and Environment, University of Leeds, Leeds, UK.

<sup>3</sup>IREA, CNR, Napoli, Italy.

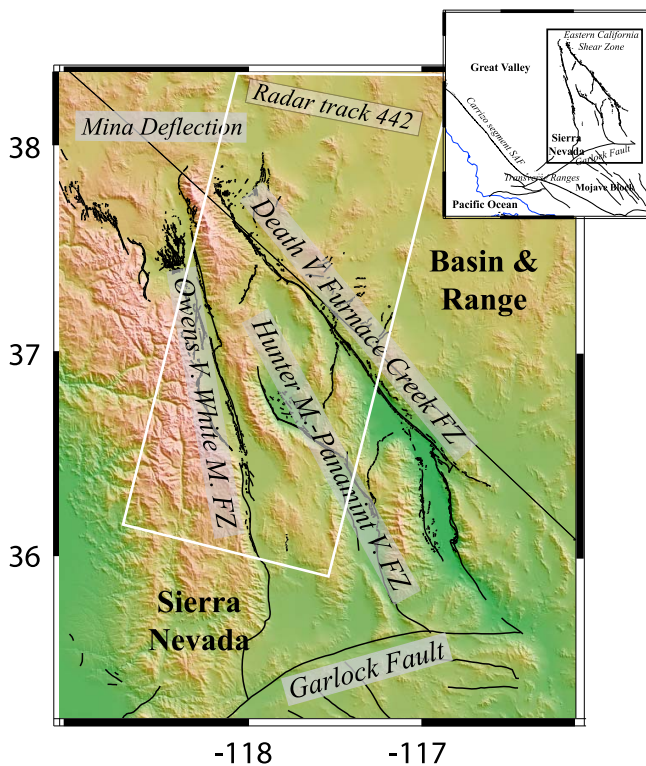


**Figure 1.** Major faults of the eastern California shear zone south of the Mina deflection and north of the Garlock fault. Location of the InSAR footprint across the ECSZ (white outline).

71 2007]. In this case, the measurement precision is limited  
72 mainly by long-wavelength phase contributions related to  
73 orbital errors (we refer to them as orbital phase errors).  
74 Burgmann *et al.* [2006] estimate a gradient of velocity error  
75 of 0.094 mm/yr/km from measuring residuals between  
76 CGPS and PS-InSAR velocity map. This gradient equates to  
77 1 cm/yr over a 100 km distance, well in the range of many  
78 strike-slip faults.

79 [5] Subtle, long-wavelength deformation can be resolved  
80 using a priori information about the surface displacement  
81 field. For example, Peltzer *et al.* [2001] calibrate InSAR  
82 data across the eastern California shear zone using a model  
83 of long-term plate motion. Fialko [2006] uses more than  
84 50 GPS velocities to remove a linear ramp from a stack of  
85 interferograms for the southern San Andreas fault. Burgmann  
86 *et al.* [2006], working in the San Francisco Bay Area, use a  
87 GPS-constrained tectonic model to remove a ramp from the  
88 InSAR velocities obtained using persistent scatterer methods.

89 [6] Various methods have been used to account for orbital  
90 phase errors. If a priori information about the displacement  
91 field is not available, long-wavelength deformation can be  
92 retrieved by simultaneous inversion for models for the tec-  
93 tonic deformation and for the orbital phase errors [Wright  
94 *et al.*, 2004; Biggs *et al.*, 2007]. In most studies, the orbital  
95 phase errors are approximated by a first-order or second-  
96 order two-dimensional polynomial. The ROI\_PAC soft-  
97 ware package from the Jet Propulsion Laboratory [Rosen

et al., 2004] uses a realistic orbital model and topographic 98 information to estimate the orbital phase errors. Kohlhase 99 *et al.* [2003] remove the orbital phase errors using an 100 orbital model and a network of SAR data. Kohlhase *et al.* 101 [2003] and Biggs *et al.* [2007] use a network approach to 102 resolve the orbital phase errors. This approach potentially 103 retains the temporal resolution of the InSAR data, although 104 Biggs *et al.* assume a linear deformation model. 105

[7] The limitations of the described methods are one or 106 more of the following: (1) they do not account for defor- 107 mation [Kohlhase *et al.*, 2003]; (2) they make assumptions 108 about the spatial variation of the deformation [Wright *et al.*, 109 2004; Biggs *et al.*, 2007]; (3) they make assumptions about 110 the time dependency of the deformation (usually assume 111 linear deformation) [Wright *et al.*, 2004]; and (4) they use 112 approximate orbital models [Wright *et al.*, 2004; Biggs *et al.*, 113 2007].

[8] In this paper, we present a new method for the mea- 115 surement of subtle, long-wavelength deformation. The 116 method identifies and removes orbital phase errors from the 117 InSAR deformation time series by using GPS and a physical 118 orbital model, without making assumptions about the dis- 119 placement field in space and time. We apply this method to 120 the eastern California shear zone, with particular emphasis 121 on the Hunter Mountain fault zone. 122

## 2. The Eastern California Shear Zone

[9] The eastern California shear zone (ECSZ), parallel to 124 the San Andreas fault system, accommodates 20%–25% of 125 the total Pacific–North American plate motion [Dokka and 126 Travis, 1990b, 1990a; Dixon *et al.*, 2000a] (Figure 1). Dur- 127 ing the past 150 years, four major earthquakes have hit the 128 region: the 1872 M8 Owens Valley, the 1932 M7.1 Cedar 129 Mountain, the 1992 M7.3 Landers, and the 1999 M7.1 130 Hector Mine Earthquakes. The Hunter Mountain fault is part 131 of the Panamint Valley–Hunter Mountain–Saline Valley 132 (PHS) system, one of the younger faults comprising the 133 ECSZ north of the Garlock fault [Lee *et al.*, 2009]. The age 134 of fault initiation is bracketed between 2.8 and 4.0 Ma [Lee 135 *et al.*, 2009; Burchfiel *et al.*, 1987; Hodges *et al.*, 1989]. The 136 total offset of the Hunter Mountain fault is estimated at  $9.3 \pm$  137 1.4 km [Burchfiel *et al.*, 1987; Sternlof, 1988] based on the 138 intersection of the Hunter Mountain batholith and the nearly 139 horizontal unconformity at the base of Miocene-Pliocene 140 volcanics; displacement of this feature across the Hunter 141 Mountain fault is mainly horizontal, consistent with strike- 142 slip motion. Published slip rates for the Hunter Mountain– 143 Panamint Valley fault system range between 2.4 and 4 mm/yr 144 [Zhang *et al.*, 1990; Oswald and Wesnousky, 2002; Dixon 145 *et al.*, 2003]. 146

## 3. Integration of InSAR Time Series With CGPS Measurements: Theory

### 3.1. Differential Interferometry

[10] Differential SAR interferometry (InSAR) is a remote 150 sensing technique that measures ground displacement by 151 exploiting the measured phase difference (usually referred to 152 as interferogram) between two SAR images acquired at 153 epochs  $t_b$  and  $t_a$  [Gabriel *et al.*, 1989; Massonnet and Feigl, 154

155 1998; Rosen *et al.*, 2000]. The raw interferogram,  $\Delta\phi_{\text{raw}}(t_b, t_a)$ ,  
156 can be represented as follows,

$$\begin{aligned}\Delta\phi_{\text{raw}}(t_b, t_a) &= \Delta\phi_{\text{def}}(t_b, t_a) + \Delta\phi_{\text{atmo}}(t_b, t_a) + \Delta\phi_{\text{orb}}(t_b, t_a) \\ &\quad + \Delta\phi_{\text{noise}}(t_b, t_a).\end{aligned}\quad (1)$$

157 The raw interferogram is a function of the phase contributions  
158 due to the ground deformation between  $t_b$  and  $t_a$ ,  $\Delta\phi_{\text{def}}(t_b, t_a)$ ;  
159 due to the difference in atmospheric delay between  $t_b$  and  $t_a$ ,  
160  $\Delta\phi_{\text{atmo}}(t_b, t_a) = \Delta\phi_{\text{atmo}}(t_b) - \phi_{\text{atmo}}(t_a)$ ; due to the orbital  
161 separation between the satellite at  $t_b$  and  $t_b$  (spatial baseline),  
162  $\Delta\phi_{\text{orb}}(t_b, t_a)$  (describing the Earth curvature and topography);  
163 and due to the phase noise,  $\Delta\phi_{\text{noise}}(t_b, t_a)$ . We consider  
164 all phase contributions to be relative quantities related to  
165 differences between the two acquisitions with the excep-  
166 tion of  $\Delta\phi_{\text{atmo}}(t_b, t_a)$ .  $\Delta\phi_{\text{atmo}}(t_b, t_a)$  can be decomposed  
167 into atmospheric contribution of each SAR acquisition  
168  $\Delta\phi_{\text{atmo}}(t_b, t_a) = \phi_{\text{atmo}}(t_b) - \phi_{\text{atmo}}(t_a)$ , with  $\phi_{\text{atmo}}(t_a)$  and  
169  $\phi_{\text{atmo}}(t_b)$  as the atmospheric delays at  $t_a$  and  $t_b$ .  $\Delta\phi_{\text{noise}}(t_b, t_a)$   
170 has components relating to particular acquisitions (thermal  
171 noise) and to the image pair (e.g., changes in the ground  
172 dielectric properties, spatial decorrelation, and processing  
173 artifacts related to interpolation and interferogram formation)  
174 [Lanari *et al.*, 2007].

175 [11] The orbital phase is modeled using information about  
176 the satellite orbits, which are only imperfectly known. The  
177 true orbital phase  $\Delta\phi_{\text{orb}}(t_b, t_a)$  is given by

$$\Delta\phi_{\text{orb}}(t_b, t_a) = \Delta\phi_{\text{orb}}^0(t_b, t_a) + \Delta\phi_{\text{orb}}^\varepsilon(t_b, t_a), \quad (2)$$

178 with  $\Delta\phi_{\text{orb}}^0(t_b, t_a)$  as the initial orbital phase based on the  
179 available satellite orbits and  $\Delta\phi_{\text{orb}}^\varepsilon(t_b, t_a)$  as the orbital phase  
180 error (OPE) related to the orbit errors and described in detail  
181 below. The differential interferogram,  $\Delta\phi(t_b, t_a)$  is obtained  
182 by subtracting the initial orbital phase from the raw inter-  
ferogram,

$$\Delta\phi(t_b, t_a) = \Delta\phi_{\text{raw}}(t_b, t_a) - \Delta\phi_{\text{orb}}^0(t_b, t_a). \quad (3)$$

183 Substitution of (1) into (3) using (2) yields the following  
184 expression for the differential interferogram,

$$\begin{aligned}\Delta\phi(t_b, t_a) &= \Delta\phi_{\text{def}}(t_b, t_a) + \Delta\phi_{\text{atmo}}(t_b, t_a) + \Delta\phi_{\text{orb}}^\varepsilon(t_b, t_a) \\ &\quad + \Delta\phi_{\text{noise}}(t_b, t_a).\end{aligned}\quad (4)$$

### 185 3.2. InSAR Time Series

186 [12] To obtain the temporal evolution of ground defor-  
187 mation, we use many SAR acquisitions of the same area and  
188 the small baseline subset (SBAS) method [Berardino *et al.*,  
189 2002; Lanari *et al.*, 2007]. In this approach, the key idea is  
190 to select interferometric pairs with small spatial and tem-  
191 poral separation in order to minimize spatial and temporal  
192 decorrelation, thus maximizing the number of temporally  
193 coherent pixels [Pepe and Lanari, 2006]. The baseline  
194 thresholds (the maximum spatial baseline and the maximum  
195 time span between acquisitions) depend on the type of  
196 environment. Sparsely vegetated environments with little

topography allow for larger thresholds than heavily vege- 197  
tated environments with significant topography. 198

[13] In the SBAS algorithm, a set of  $Q$  phase-unwrapped 199  
interferograms,  $\Delta\phi_p$ , with  $p = 1, \dots, Q$ , is generated from a 200  
sequence of  $N$  acquisitions at epochs  $(t_1, \dots, t_N)$ . These in- 201  
terferograms are subsequently inverted for the phase at 202  
epoch  $t_i$  with respect to the first acquisition  $\phi(t_1)$ , 203

$$\phi(t_i) = \phi_{\text{def}}(t_i) + \phi_{\text{atmo}}(t_i) + \phi_{\text{orb}}^\varepsilon(t_i) + \phi_{\text{noise}}(t_i), \quad (5)$$

with  $i = 2, \dots, N$ ,

with  $\phi_{\text{def}}(t_i)$ ,  $\phi_{\text{atmo}}(t_i)$ ,  $\phi_{\text{orb}}^\varepsilon(t_i)$ , and  $\phi_{\text{noise}}(t_i)$  as the phase due 204  
to deformation, atmosphere orbital error, and noise with 205  
respect to the first acquisition, respectively. The phase 206  
contributions at the first epoch cannot be estimated because 207  
of the rank deficiency of the system.  $\phi_{\text{noise}}(t_i)$  now also 208  
contains phase-unwrapping errors. Note that interferograms 209  
including the first acquisition directly measure  $\phi(t_i)$ , 210

$$\phi(t_i) = \Delta\phi(t_i, t_1), \quad (6)$$

and similarly for  $\phi_{\text{def}}(t_i)$ ,  $\phi_{\text{atmo}}(t_i)$ ,  $\phi_{\text{orb}}^\varepsilon(t_i)$ , and  $\phi_{\text{noise}}(t_i)$ . 211  
Throughout the remainder of this paper, we only consider 212  
phase contributions with respect to the first acquisition. 213

[14] The objective of crustal deformation studies is to 214  
recover  $\phi_{\text{def}}(t_i)$  from the retrieved  $\phi(t_i)$ , thus requiring the 215  
estimation of  $\phi_{\text{noise}}(t_i)$ ,  $\phi_{\text{atmo}}(t_i)$ , and  $\phi_{\text{orb}}^\varepsilon(t_i)$ , which is 216  
described in the next three sections. 217

### 218 3.3. Temporal Coherence

[15] The phase noise  $\phi_{\text{noise}}(t_i)$  is quantified using the 219  
temporal coherence. The SBAS analysis is typically carried 220  
out using spatially averaged (multilooked) interferograms 221  
[Rosen *et al.*, 2000]. We select the coherent pixels for each 222  
multilooked interferograms by computing the spatial 223  
coherence; the coherent pixels are then used to phase- 224  
unwrap each interferogram before inversion for  $\phi(t_i)$ . For 225  
each pixel, we then compute a temporal coherence factor 226  
defined as, 227

$$\gamma = \frac{\left| \sum_{p=1}^Q \exp[j(\Delta\phi_p - \overline{\Delta\phi_p})] \right|}{Q}, \quad 0 \leq \gamma \leq 1, \quad (7)$$

where  $\Delta\phi_p$  is the phase of the original  $p$ th interferogram 228  
and  $\overline{\Delta\phi_p}$  is the phase of the corresponding synthetic 229  
interferogram generated by differencing the phase of the 230  
computed time series for the two epochs of the  $p$ th inter- 231  
ferogram. Low temporal coherence arises from incon- 232  
sistencies of the phase between original and synthetic 233  
interferograms. The main causes are decorrelation effects 234  
and errors during phase unwrapping of the interferograms. 235  
For pixels with  $\gamma \rightarrow 1$ , we expect no errors since a nearly 236  
perfect retrieval of the original phase has been obtained. In 237  
the following we consider only pixel with gamma above a 238  
certain threshold. For these pixels, we assume  $\phi_{\text{noise}}(t_i) = 0$  239  
for  $i = 1, \dots, N$  and equation (5) simplifies to 240

$$\phi(t_i) = \phi_{\text{def}}(t_i) + \phi_{\text{atmo}}(t_i) + \phi_{\text{orb}}^\varepsilon(t_i), \quad \text{with } i = 2, \dots, N. \quad (8)$$

### 241 3.4. Atmospheric Filtering

242 [16] The atmospheric phase  $\phi_{\text{atmo}}(t_i)$  is the difference  
 243 between the atmospheric phase screen at epoch  $t_i$  and at the  
 244 epoch of the first acquisition  $t_1$ . The atmospheric phase  
 245 screen is estimated using a spatial-temporal filter [Ferretti  
 246 et al., 2001; Berardino et al., 2002], assuming that atmo-  
 247 spheric phase contributions are spatially correlated and tem-  
 248 porally uncorrelated. We apply a low-pass spatial filter  
 249 followed by a high-pass temporal filter to  $\phi(t_i)$ . We assume  
 250 that the estimated atmospheric phase screen  $\hat{\phi}_{\text{atmo}}(t_i)$  equals  
 251 the atmospheric phase screen  $\phi_{\text{atmo}}(t_i)$ , i.e., that the atmo-  
 252 spheric phase screen errors  $\phi_{\text{atmo}}^{\varepsilon}(t_i)$  is negligible. We retrieve  
 253 the atmospheric phase screen at the epoch of the first acqui-  
 254 sition assuming that the atmospheric phase screens has zero  
 255 mean,

$$\phi_{\text{atmo}}(t_1) \approx \frac{1}{N-1} \sum_{i=2}^N \hat{\phi}_{\text{atmo}}(t_i). \quad (9)$$

256 Subtraction of  $\phi_{\text{atmo}}(t_i)$  from  $\phi(t_i)$  leads to the filtered phase  
 257 with respect to the first acquisition  $\phi_{\text{filt}}(t_i)$ ,

$$\phi_{\text{filt}}(t_i) = \phi(t_i) - \phi_{\text{atmo}}(t_i). \quad (10)$$

258 Substituting (10) into (8) gives

$$\phi_{\text{filt}}(t_i) = \phi_{\text{def}}(t_i) + \phi_{\text{orb}}^{\varepsilon}(t_i), \text{ with } i = 2, \dots, N. \quad (11)$$

### 259 3.5. Orbital Phase Error

260 [17] The initial orbits used for InSAR processing of ERS-1  
 261 and ERS-2 satellites deviate from the true orbits by about  
 262 15 cm on average [Scharroo, 2002]. The initial orbit, at epoch  
 263  $t_i$ ,  $o^0(t_i)$ , relates to the true orbit,  $o(t_i)$ , as

$$o(t_i) = o^0(t_i) + o^{\varepsilon}(t_i), \quad (12)$$

264 with  $o^{\varepsilon}(t_i)$  as the orbital error we are seeking to estimate. In  
 265 practice, the spatial separation between the satellites during  
 266 image acquisition (baseline) is used. For an interferogram  
 267 between SAR images at epochs  $t_b$  and  $t_a$ , the baseline  $b(t_b, t_a)$   
 268 is given by  $b(t_b, t_a) = \Delta o(t_b, t_a) = o(t_b) - o(t_a)$ . The baseline at  
 269 epoch  $t_i$ ,  $b(t_i)$ , is the difference between the orbit at epoch  $t_i$   
 270 and the orbit of the first acquisition  $o(t_1)$ ,

$$b(t_i) = o(t_i) - o(t_1), \quad (13)$$

271 with  $i = 2, \dots, N$ . The initial baseline at epoch  $t_i$ ,  $b^0(t_i)$ , relates  
 272 to the true baseline,  $b(t_i)$ , as

$$b(t_i) = b^0(t_i) + b^{\varepsilon}(t_i), \quad (14)$$

273 with  $b^{\varepsilon}(t_i)$  as the baseline error. The baseline error relates to  
 274 the orbital error as

$$b^{\varepsilon}(t_i) = o^{\varepsilon}(t_i) + o^{\varepsilon}(t_1). \quad (15)$$

275 [18] The orbital phase  $\phi_{\text{orb}}(t_i)$  at epoch  $t_i$  (due to the Earth  
 276 curvature and topography) is linearly related to the baseline  
 277 [Hanssen, 2001, equation (2.4.18)],

$$\phi_{\text{orb}}(t_i) = b_h(t_i)F_h - b_v(t_i)F_v, \quad (16)$$

with  $b_h$  and  $b_v$  as the horizontal and vertical baseline com-  
 277 ponents, respectively, and  $F_{h,v}$  as two factors as  
 278

$$F_h = \left(4 \frac{\pi}{\lambda}\right) \left(\sin \vartheta - \frac{\cos \vartheta}{\sin \vartheta} \frac{H}{R}\right) \text{ and} \quad (17)$$

$$F_v = \left(4 \frac{\pi}{\lambda}\right) \left(-\cos \vartheta - \frac{H}{R}\right). \quad (18)$$

279  $H$  is the terrain height above the ellipsoid,  $R$  is the distance  
 280 between the ground and the satellite (range), and  $\vartheta$  is the  
 281 angle at which the radar looks at the surface (look angle).

282 [19] The initial orbital phase based on the initial orbits  
 283  $\phi_{\text{orb}}^0(t_i)$  relates to the true orbital phase  $\phi_{\text{orb}}(t_i)$  as

$$\phi_{\text{orb}}(t_i) = \phi_{\text{orb}}^0(t_i) + \phi_{\text{orb}}^{\varepsilon}(t_i), \quad (19)$$

284 with  $\phi_{\text{orb}}^{\varepsilon}(t_i)$  as the orbital phase error. We thus can express  
 285 the orbital phase error in terms of the horizontal and vertical  
 286 baseline errors,  $b_h^{\varepsilon}(t_i)$  and  $b_v^{\varepsilon}(t_i)$ , as

$$\phi_{\text{orb}}^{\varepsilon}(t_i) = b_h^{\varepsilon}(t_i)F_h - b_v^{\varepsilon}(t_i)F_v. \quad (20)$$

287 The task is to estimate  $b_h^{\varepsilon}(t_i)$  and  $b_v^{\varepsilon}(t_i)$  from which  $b_{\text{orb}}^{\varepsilon}(t_i)$   
 288 can be estimated.

#### 289 3.5.1. OPE Estimation in the Presence of Deformation

290 [20] We estimate  $b_h^{\varepsilon}(t_i)$  and  $b_v^{\varepsilon}(t_i)$  at each epoch  $t_i$  by  
 291 minimizing:

$$\min \{ \phi_{\text{filt}}(t_i) - \phi_{\text{def}}(t_i) - \phi_{\text{orb}}^{\varepsilon}(t_i) \}. \quad (21)$$

291 In the absence of deformation, i.e., for  $\phi_{\text{def}}(t_i) = 0$ , we  
 292 estimate  $b_h^{\varepsilon}(t_i)$  and  $b_v^{\varepsilon}(t_i)$  from  $\phi_{\text{filt}}(t_i)$  (i.e., from InSAR  
 293 only). In the presence of deformation, we estimate  $b_h^{\varepsilon}(t_i)$  and  
 294  $b_v^{\varepsilon}(t_i)$  using a priori information on  $\phi_{\text{def}}(t_i)$  as described  
 295 below. Note that in the classical SBAS approach [Berardino  
 296 et al., 2002] it is assumed that  $\phi_{\text{orb}}^{\varepsilon}(t_i)$  is a simple linear  
 297 function which is estimated and then removed from  $\phi_{\text{filt}}(t_i)$ .

298 [21] Continuous GPS measurements provide displacement  
 299 at epoch  $t_i$ , at radar range location  $r$  and radar azimuth  
 300 location  $a$ ,  $\phi_{\text{def}}(t_i, r, a)$ . Because of the pointwise nature of  
 301 CGPS measurements and the number of available CGPS  
 302 stations in the InSAR footprint, we approximate the along-  
 303 track variation of  $b_h^{\varepsilon}(t_i)$  and  $b_v^{\varepsilon}(t_i)$  by second-order poly-  
 nomials,

$$b_h^{\varepsilon}(t_i) = c_1(t_i)a^2 + c_2(t_i)a + c_3(t_i), \quad (22)$$

$$b_v^{\varepsilon}(t_i) = c_4(t_i)a^2 + c_5(t_i)a + c_6(t_i), \quad (23)$$

304 with  $a$  as the azimuth coordinate. Equation (20) takes the  
 305 form

$$\begin{aligned} \phi_{\text{orb}}^{\varepsilon}(t_i) &= (c_1(t_i)a^2 + c_2(t_i)a + c_3(t_i))F_h \\ &\quad - (c_4(t_i)a^2 + c_5(t_i)a + c_6(t_i))F_v. \end{aligned} \quad (24)$$

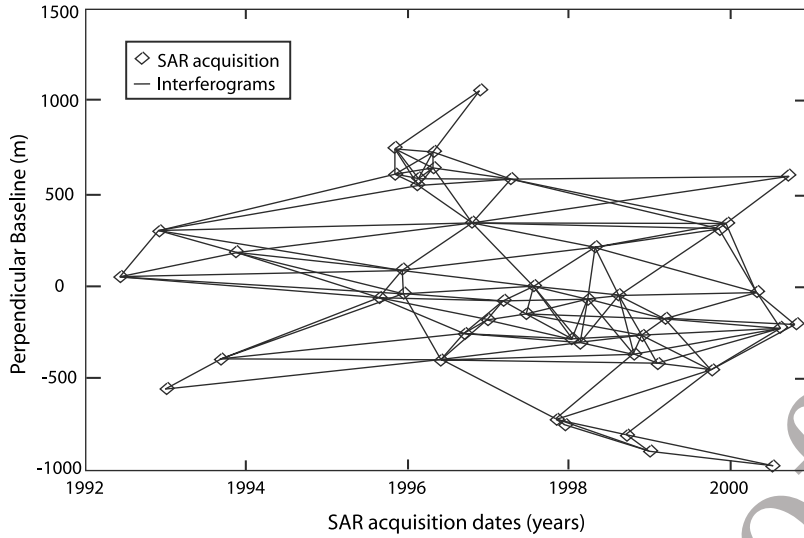


**Figure 2.** Perpendicular and temporal baselines of SAR acquisitions used in this study. Line segments represent the network of interferograms used for the time series inversion.

[22] At each epoch,  $\phi_{\text{orb}}^{\varepsilon}(t_i)$  is thus described by six parameters,  $c_1, \dots, c_6$ ; thus, we estimate  $b_h^{\varepsilon}(t_i)$  and  $b_v^{\varepsilon}(t_i)$  by minimizing,

$$\min \left\{ \sum_{m=1}^M (\phi_{\text{filt}}(t_i, r_m, a_m) - \phi_{\text{def}}(t_i, r_m, a_m) - \phi_{\text{orb}}^{\varepsilon}(t_i, r_m, a_m))^2 \right\}. \quad (25)$$

[23] If deformation is known at six locations ( $m = 6$ ), we solve a system of six equations with the six unknowns  $c_1, \dots, c_6$  at each epoch  $t_i$ . Note that the estimation of  $\phi_{\text{orb}}^{\varepsilon}(t_i)$  and  $b_h^{\varepsilon}(t_i)$  is associated with errors,

$$\phi_{\text{orb}}^{\varepsilon}(t_i) = \hat{\phi}_{\text{orb}}^{\varepsilon}(t_i) + \phi_{\text{orb}}^{\varepsilon\varepsilon}(t_i), \quad (26)$$

$$b_h^{\varepsilon}(t_i) = \hat{b}_h^{\varepsilon}(t_i) + b_h^{\varepsilon\varepsilon}(t_i), \quad (27)$$

[24] with  $\hat{\phi}_{\text{orb}}^{\varepsilon}(t_i)$  and  $\hat{b}_h^{\varepsilon}(t_i)$  as the estimated orbital phase error and baseline component errors, respectively, and  $\phi_{\text{orb}}^{\varepsilon\varepsilon}(t_i)$  and  $b_h^{\varepsilon\varepsilon}(t_i)$  as the respective estimation errors.

[25] After subtraction of  $\phi_{\text{orb}}^{\varepsilon}(t_i)$  from  $\phi_{\text{filt}}(t_i)$ , we have achieved our objective of recovering  $\phi_{\text{def}}(t_i)$ .

#### 4. Integration of InSAR Time Series and CGPS: Application to ECSZ

##### 4.1. Large-Scale SBAS Processing

[26] In the past, the SBAS technique has mostly been applied to investigate deformation of areas typically extending  $\sim 100 \times 100 \text{ km}^2$ . In this study, we use the SBAS technique to study a larger area ( $\sim 600 \times 100 \text{ km}^2$ ) [Casu et al., 2008].

[27] We analyze a set of 44 ERS-1/2 SAR swaths (track 442, frames 2781–2871), spanning the 1992–2000 time interval. To reduce the amount of data to be processed, the image resolution is degraded to a pixel size of  $160 \times 160 \text{ m}^2$  compared to  $80 \times 80 \text{ m}^2$  for conventional SBAS processing.

[28] The interferometric pairs are selected using a maximum spatial and temporal baseline of 400 m and 1500 days, respectively (Figure 2); by applying these constraints, 148 multilook interferograms are generated. The interferograms are phase-unwrapped and subsequently inverted for the phase with respect to the first acquisition  $\phi(t_i)$ .

##### 4.2. Temporal Coherence

[29] The temporal coherence estimated using equation (7) is shown in Figure 3a. Most of the low-topography areas, including the basins, exhibit high coherence (larger than 0.7). The mountain ranges are characterized by low coherence (near 0), including the Sierra Nevada in the southwest. The loss of coherence occurs because the surface characteristics change with time. In the mountains, coherence is lost because of temporary snow cover. In some valleys, coherence may be lost because of flooding. Another reason for coherence loss in the mountains is geometric decorrelation related to the steep slopes. In this study, we use only pixel with temporal coherence larger than 0.7 shown in Figure 3b.

##### 4.3. Atmospheric Filtering

[30] In order to quantify the efficiency of the atmospheric filtering, we perform a 1-D covariance analysis [Hanssen, 2001] on the phase before and after filtering ( $\phi(t_i)$  and  $\phi_{\text{filt}}(t_i)$ , respectively). At each epoch, we conduct an auto-correlation and model the resulting amplitude by a two-parameter Bessel function following Biggs et al. [2007] (Figures 4a and 4b). Figure 4 shows that the spatial-temporal filtering reduces the correlation amplitude and length in average by 30%.

[31] The atmospheric filtering is illustrated in map view in Figure 5. Figure 5 shows the phase at the 23 November 1992 epoch before and after filtering (Figures 5a and 5d, respectively) as well as the estimated  $\phi_{\text{atmo}}(t_i)$  for the first acquisition (1 June 1992, Figure 5b) and for the 23 November 1992 acquisition (Figure 5c). The phase at epoch 23 November 1992 corresponds to the interferogram

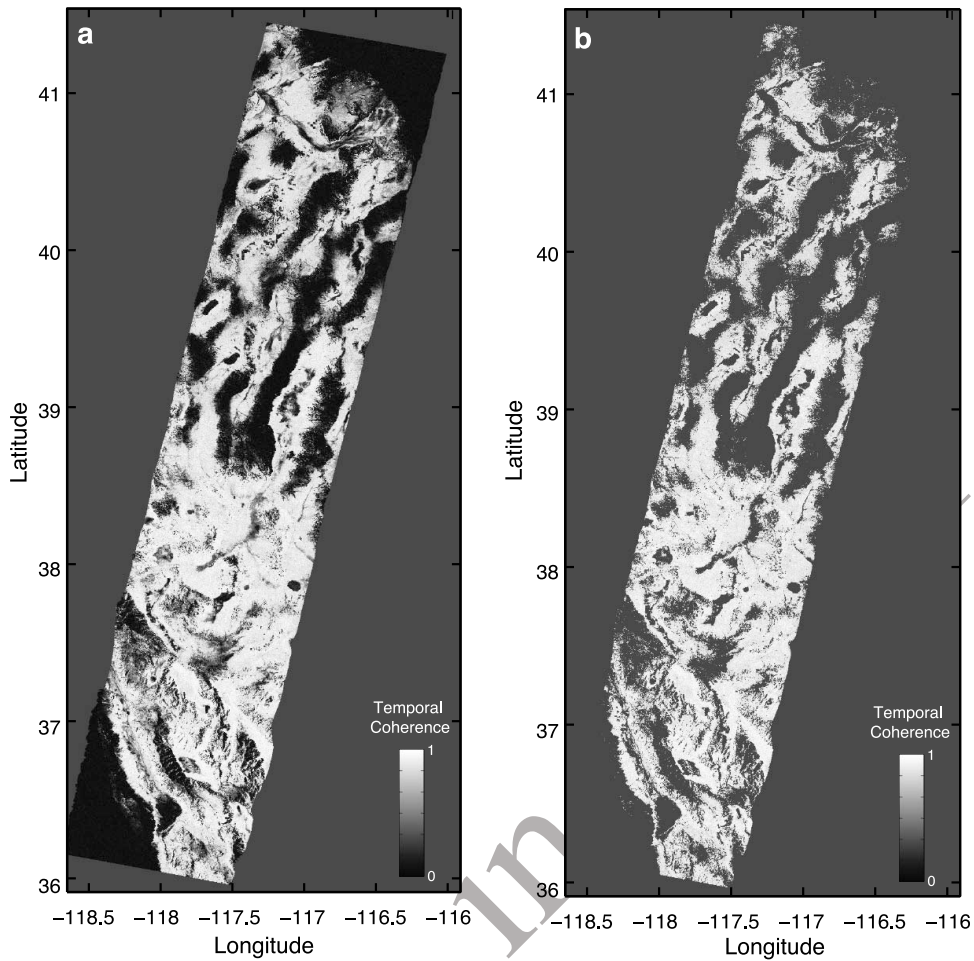


**Figure 3.** (a) Temporal coherence  $\gamma$ . (b) Coherence mask using a threshold of 0.7.

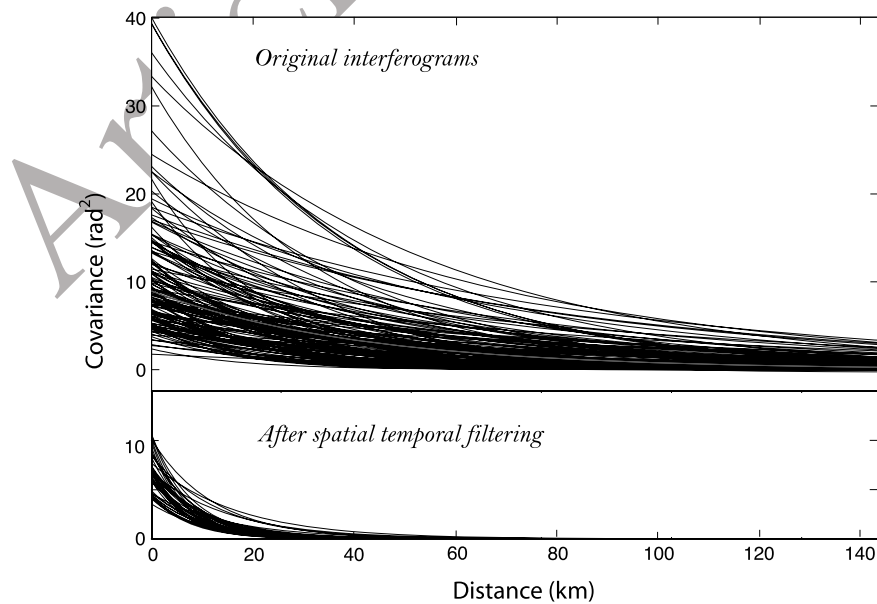


**Figure 4.** Phase covariance as a function of distance between pixel for each of the 44 epochs (a) before and (b) after spatial-temporal filtering. The filtering reduces both the magnitude and length of the correlated noise by about 40%.

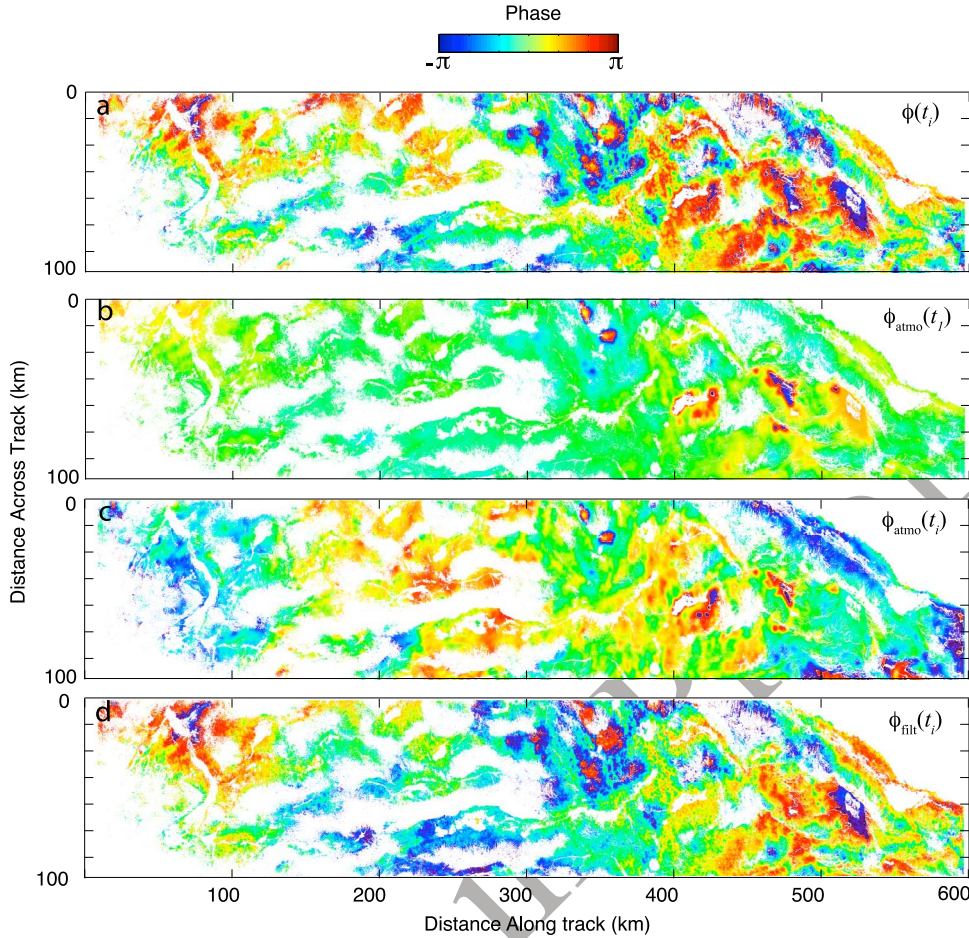


**Figure 5.** Example of the phase at a given epoch before and after atmospheric filtering: (a) phase before atmospheric filtering at epoch  $t_i = 23$  November 1992,  $\phi(t_i)$ ; (b) estimated atmospheric phase screen for reference epoch  $t_1 = 1$  June 1992,  $\phi_{\text{atmo}}(t_1)$ ; (c) estimated atmospheric phase screen for epoch  $t_i = 23$  November 1992,  $\phi_{\text{atmo}}(t_i)$ ; and (d) filtered phase at epoch  $t_i = 23$  November 1992 obtained using equation (10),  $\phi_{\text{filt}}(t_i)$ .

366 between the 6 June 1992 and 23 November 1992 acquisitions because the first acquisition of the interferogram is also  
 367 the reference epoch of the time series (see equation (10)).  
 368 [31] The estimated baseline error for the 23 November  
 369 1992 epoch with and without atmospheric filtering is shown  
 370 in Figure 6. The differences are generally only a few centimeters,  
 371 with several meters locally, indicating that atmospheric  
 372 filtering has only little effect on the estimated  
 373 baseline error.  
 374

#### 4.4. Baseline Errors and the Effect of Ground Deformation on Their Estimation

375  
376

[32] The baseline errors for five epochs, estimated using  
 377 the assumption of no deformation,  $\phi_{\text{def}}(t_i) = 0$ , are shown as  
 378 function of azimuth in Figure 7. The estimated baseline  
 379 errors ( $\hat{b}_h^{\varepsilon}(t_i)$  and  $\hat{b}_v^{\varepsilon}(t_i)$ ) along most of the SAR swath is less  
 380 than 15 m (Figures 7a and 7b). This is much larger than the  
 381 orbital error estimates of Scharroo [2002], but similar to  
 382 values obtained using the baseline reestimation  
 383

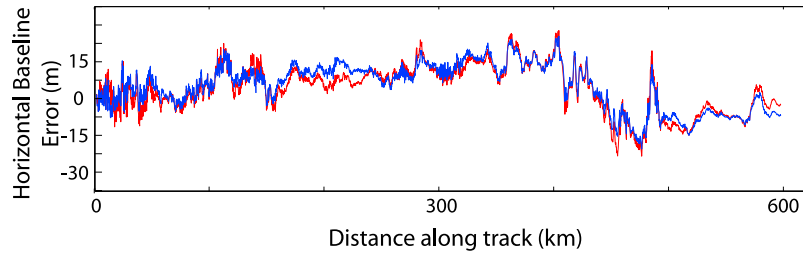


**Figure 6.** Horizontal baseline error at epoch  $t_i = 23$  November 1992,  $\hat{b}_h^{\varepsilon}(t_i)$ , obtained from equation (21) and substituting equation (20) before (red line) and after atmospheric filtering (blue line), assuming  $\phi_{\text{def}}(t_i) = 0$ .

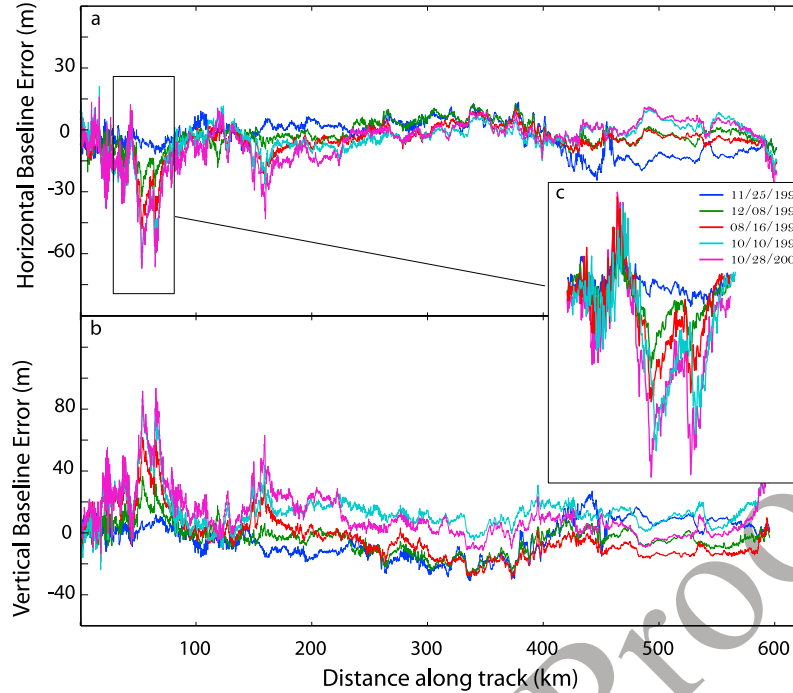


**Figure 7.** (a) Horizontal and (b) vertical baseline error,  $\hat{b}_{h,v}^e(t_i)$ , for five example epochs estimated assuming  $\phi_{def}(t_i) = 0$ . (c) Zoom into horizontal baseline error for the subsiding Crescent Valley area (see Figure 13) and epochs of SAR acquisitions. The large variations of the estimated baseline error in the subsidence area illustrate that deformation needs to be taken into account for baseline error estimation.

384 strategy based on topographic information used in JPL's  
 385 ROI\_PAC software [Rosen *et al.*, 2004]. At the beginning  
 386 of the SAR swath (at 40–100 km along-track distance,  
 387 Figure 7c) and at the end of the swath (at 400–600 km  
 388 along-track distance), the estimated baseline error is up to  
 389 60 and 30 m, respectively (Figure 7c). This is caused by the  
 390 assumption that  $\phi_{def}(t_i) = 0$ . The effect of surface displace-  
 391 ment on the estimated baseline error is clearly illustrated by  
 392 the retrieved baseline correction term in the subsiding region  
 393 of the Crescent Valley area (Figure 8), where we see a linear  
 394 correlation between the estimated baseline error  $\hat{b}_h^e(t_i)$  and  
 395 the surface deformation  $\phi_{def}(t_i)$ . We conclude from this  
 396 section that  $\phi_{def}(t_i)$  needs to be taken into account for the  
 397 estimation of the baseline errors.

#### 398 4.5. OPE Estimation Using GPS

##### 399 4.5.1. GPS Data

400 [33] We use continuous GPS (CGPS) as a measure of  
 401  $\phi_{def}(t_i)$ . We use six CGPS stations from the PBO core net-  
 402 work (previously referred to as BARGEN network)  
 403 [Wernicke *et al.*, 2000; Bennett *et al.*, 2003; Davis *et al.*,  
 404 2006] located in the area imaged by the SAR (Figure 9).  
 405 The stations are distributed evenly over the entire SAR  
 406 track. Two stations are located on the stable Basin and  
 407 Range block (MONI and TONO), two stations are located in  
 408 the vicinity of the Central Nevada Seismic Belt (GABB,  
 409 NEWS), and two stations are located in the vicinity of the  
 410 ECSZ (ARGU, COSO, and DYER). There are two addi-  
 411 tional GPS stations with data starting in the mid-1990s  
 412 (LEWI and COSO), but we could not use them for reasons  
 413 discussed below. The CGPS positions are referred to a  
 414 stable Basin and Range reference frame defined by 26

permanent GPS stations located within the stable Basin and 415  
 Range block [Schmalzle, 2008]. We use the GPS records 416  
 starting in 1999 when all six stations were operating 417  
 simultaneously. 418

[34] In the following, we consider the GPS displacement 419  
 component in radar line-of-sight (LOS) direction, obtained 420

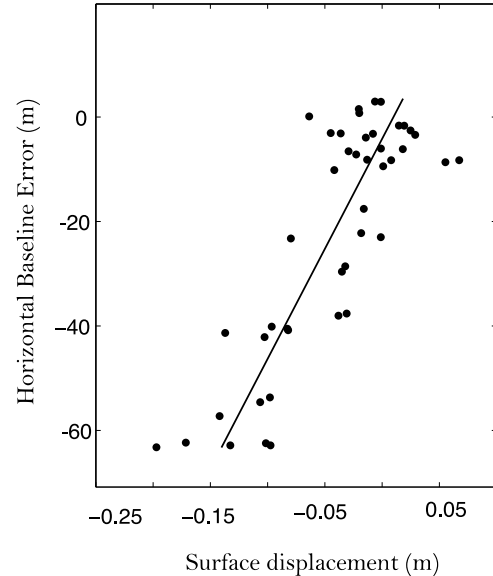


**Figure 8.** Horizontal baseline errors for all epochs  $\hat{b}_h^e(t_i)$  estimated assuming  $\phi_{def}(t_i) = 0$  versus surface displacement and linear fit for a pixel in the subsiding Crescent Valley area (at 70 km distance along track on Figure 7).

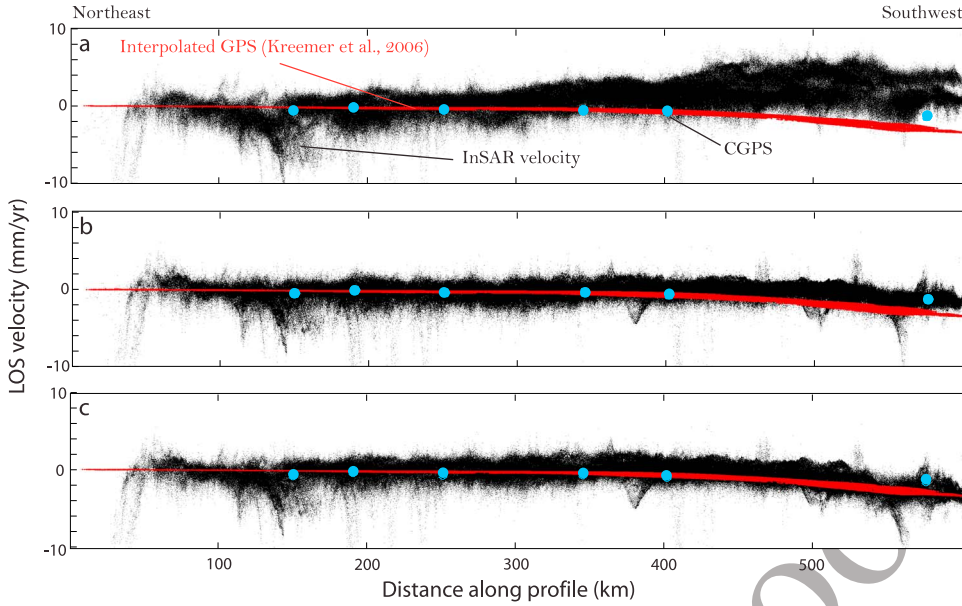


**Figure 9.** GPS velocity (red and blue) and InSAR velocity (black) in LOS direction projected along a profile perpendicular to the ECSZ (see Figure 13) for location of the profile between 300 and 600 km: (a) InSAR velocity without OPE removal, (b) InSAR velocity with OPE removal not accounting for deformation, and (c) InSAR velocity with OPE removal using the CGPS measurements to account for deformation. LOS velocity of the six CGPS stations used in the inversion (blue dots). At a distance along the profile of 0 km, the InSAR, GPS, and CGPS profiles have been arbitrarily adjusted to 0 mm/yr.

421 by multiplying the east, north, up GPS vector with the unit  
422 vector pointing from the ground to the radar [0.3, -0.09,  
423 0.9] in [east, north, up].

#### 424 4.5.2. GPS Velocity Field

425 [35] For the comparison of the InSAR with the GPS, we  
426 use the interpolated horizontal velocity field of the Basin  
427 and Range region from the work of Kreemer *et al.* [2006].  
428 This velocity field is based on campaign and continuous  
429 data with records of a few years to over 15 years with large  
430 station density variations (the station density is higher near  
431 the active volcanic and seismic region of the Sierra Nevada–  
432 Basin and Range boundary). The GPS velocity field includes  
433 data of the high-density, semipermanent MAGNET network  
434 operated by the University of Nevada, Reno. Kreemer *et al.*  
435 obtained this spatially continuous velocity field (on a  $0.2^\circ \times$   
436  $0.2^\circ$  grid) from the GPS point measurements by interpolat-  
437 ing the GPS velocities in a least squares sense using a bi-  
438 cubic Bessel spline function. For the analysis below this  
439 velocity field is transformed into LOS direction assuming  
440 zero vertical deformation.

#### 441 4.5.3. Comparison Between InSAR and Interpolated 442 GPS Velocity Field

443 [36] To illustrate the effect of OPE on the calculated In-  
444 SAR ground velocity and time series, we compare the  
445 ground velocity data from InSAR with continuous GPS and  
446 the interpolated GPS velocity field. To do so, we project all  
447 data sets (LOS component for the GPS) along a profile per-  
448 pendicular to the ECSZ (in N60°W direction) (Figure 9). The  
449 InSAR data are shown without OPE removal (Figure 9a),  
450 with OPE removal assuming zero deformation (Figure 9b),  
451 and with OPE removal accounting for deformation using the  
452 continuous GPS data (Figure 9c).

[37] Without OPE removal, there is a general disagree- 453  
ment between the InSAR and GPS (Figure 9a). At 400– 454  
600 km along the profile, the difference is on the order of 4– 455  
8 mm/yr. The nature of the velocity difference is similar to 456  
the work of Burgmann *et al.* [2006], although we observe a 457  
lower gradient, 0.03 mm/yr/km. With OPE removal 458  
assuming zero deformation, the InSAR and GPS data are 459  
roughly consistent in the northeast (0–400 km along pro- 460  
file), but there is a discrepancy in the southeast of about 2– 461  
3 mm/yr (Figure 9b). Note that scatter is less when the OPE 462  
is removed (Figure 9b compared with Figure 9c). The case 463  
of OPE removal accounting for deformation (Figure 9c) is 464  
discussed below. 465

#### 466 4.5.4. Comparison Between InSAR and Continuous 467 GPS

[38] The CGPS stations are located within the mountain 468  
ranges, where InSAR data are not available because of 469  
decorrelation. We therefore average all coherent InSAR 470  
pixel within 2 km radius from each CGPS stations. As a 471  
result, we have to eliminate the LEWI and COSO GPS 472  
stations from our analysis. Both stations are affected by 473  
local deformation and therefore the ground within 2 km 474  
from the GPS bench mark may deform differently than the 475  
GPS bench mark itself. LEWI is affected by local subsidence 476  
due to water withdrawal in support of mining activities 477  
[Gourmelen *et al.*, 2007]; COSO is affected by subsidence 478  
associated with the nearby Coso geothermal plant [Bennett 479  
*et al.*, 2003]. We note that GPS stations affected by local 480  
deformation can be used for the estimation of orbital phase 481  
errors as long as they collocate with coherent pixel. 482

[39] The InSAR time series are shown together with the 483  
CGPS time series in Figure 10a for the six GPS stations. The 484  
northernmost stations are plotted at the top and the south- 485

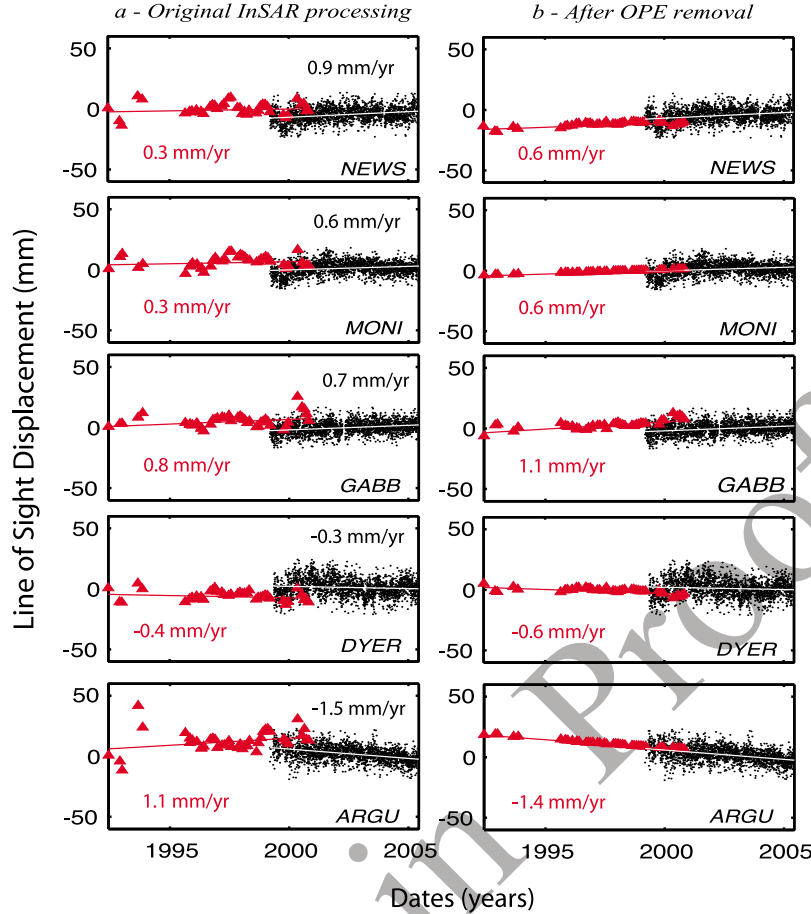


**Figure 10.** LOS displacement time series from InSAR SBAS analysis and daily positions for six collocated GPS sites in the western Basin and Range. (a) Conventional SBAS analysis after the removal of linear and second-order phase contributions (before calibrations with GPS). (b) SBAS analysis after removal of OPE determined from continuous GPS measurements. We extrapolated the 1999–2005 GPS measurements back to the beginning of SAR measurements in 1992. The InSAR errors are estimated at  $\pm 0.6$  mm/yr [Gourmelen et al., 2007]; GPS errors of  $\pm 0.7$  are estimated assuming white and flicker noise [Dixon et al., 2000b].

486 ernmost stations at the bottom of the frame. The largest  
487 differences between InSAR and GPS are found in the  
488 southernmost areas, within the ECSZ. For example,  
489 ARGU's GPS velocity is  $-1.5 \pm 0.7$  mm/yr, whereas the  
490 corresponding InSAR velocity is  $+1.1 \pm 0.6$  mm/yr, a dif-  
491 ference of 2.6 mm/yr. To the north within the stable Basin  
492 and Range block MONI's GPS velocity is  $0.6 \pm 0.7$  mm/yr,  
493 whereas the corresponding InSAR velocity is  $0.3 \pm 0.6$  mm/yr,  
494 a difference of 0.3 mm/yr. This pattern of southwestward  
495 increasing differences between InSAR and continuous GPS  
496 is similar to differences between the InSAR and the inter-  
497 polated GPS velocity field from Kreemer et al. [2006]  
498 (Figure 9).

#### 4.5.5. OPE Correction Using Continuous GPS

[40] The continuous GPS data are complete since 1999  
501 but the InSAR data start in 1992. Therefore, we extrapolate  
502 the GPS time series for the 1992–1999 period using the  
503 averaged 1999–2005 velocities. This approach yields pre-  
504 dicted GPS positions at each SAR epoch.

[41] We then assume a second order azimuth model and  
505 apply equation (25) to estimate the OPE and remove it from

the InSAR time series at each epoch. The corrected InSAR 507  
time series show a significant reduction of the noise level 508  
(Figure 10, right). More importantly, the difference between 509  
the InSAR and continuous GPS velocities is within the 510  
range of error. 511

[42] The quality of the OPE estimation using GPS is also 512  
clearly seen by comparing the InSAR with the interpolated 513  
GPS velocity field of Kreemer et al. [2006]. After OPE 514  
removal accounting for deformation (Figure 9c), there is a 515  
broad agreement between the InSAR velocities and the 516  
interpolated GPS velocities. 517

#### 4.5.6. Azimuth Model

[43] To evaluate the spatial model used to approximate the 519  
OPE, we compute the standard deviation of the phase his- 520  
tory for each pixel. Figure 11 shows the standard deviation 521  
for the original time series (Figure 11a), after removal of the 522  
OPE assuming a linear azimuth model (obtained by substi- 523  
tuting equations (22) and (23) by a linear model (Figure 11b) 524  
and after removal of the OPE using the quadratic models of 525  
equations (22) and (23) (Figure 11c). We also display the 526  
phase of the 23 November 1992 epoch as a function of the 527

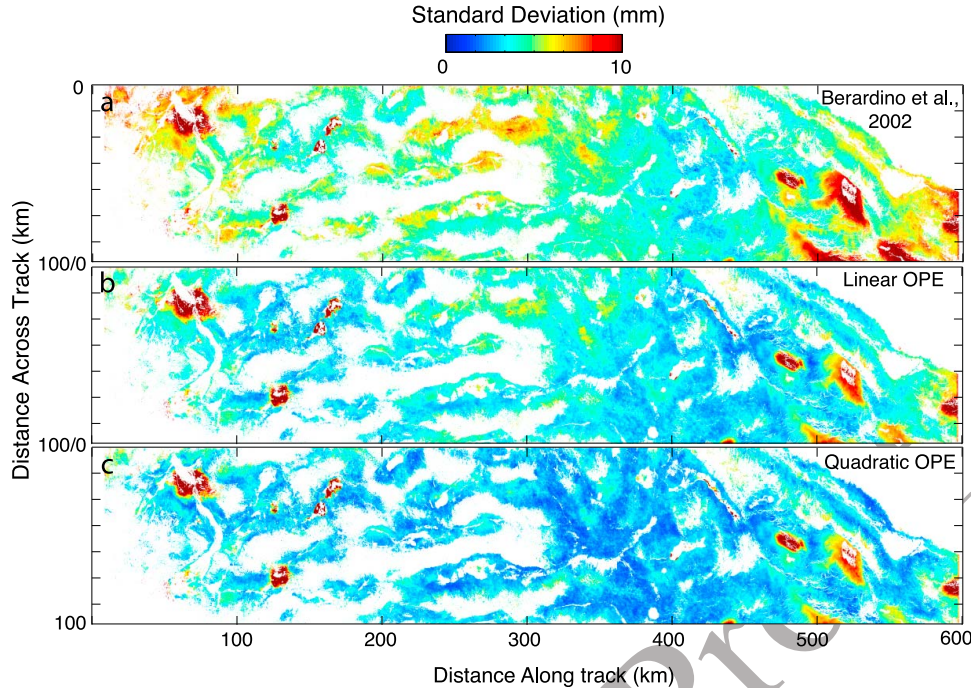


**Figure 11.** Standard deviation of the time series in function of the orbital model. Quadratic variation of the baseline errors gives the most satisfying results. High residual standard deviation is localized and corresponds to regions of deformation (e.g., subsidence, earthquakes).

528 model used to remove the OPE (Figure 12). The quadratic  
 529 model results in the smallest standard deviation and per-  
 530 forms well in removing long-wavelength phase residuals,  
 531 suggesting that a quadratic model is most appropriate.  
 532 However, the standard deviation criteria has to be taken with  
 533 caution as strong regional periodical signal typically recorded  
 534 by GPS, from atmospheric or hydrologic forcing, will tend to  
 535 increase the standard deviation. These effects are minimized  
 536 as we consider the GPS record in a local reference frame  
 537 where atmospheric or hydrologic forcing are homogeneous.  
 538 Local deformation due to subsidence or earthquakes is  
 539 associated with a high standard deviation in the three cases  
 540 as expected.

#### 541 **4.5.7. InSAR Velocity Map**

542 [44] The average velocity for each coherent pixel, obtained  
 543 from the filtered time series, is shown in Figure 13. Tight-  
 544 ening the color scale between  $[-4, 4]$  mm/yr reveals the  
 545 pattern of deformation across the ECSZ (Figure 14). Little  
 546 deformation is seen across the Fish Lake Valley–Furnace  
 547 Creek fault system. Assuming pure strike-slip motion across  
 548 the fault, taking into account the orientation of the fault with  
 549 respect to the radar look angle, and the InSAR rate uncer-  
 550 tainty of 0.6 mm/yr, we can determine an upper limit of  
 551 2 mm/yr of strain accumulation across the fault system. This  
 552 upper limit can be higher however depending on the  
 553 deformation’s wavelength. The velocity map reveals a sharp  
 554 and localized deformation along the White Mountain fault;  
 555 the deformation is localized along a narrow band in the  
 556 central part of the valley and corresponds to ground subsi-  
 557 dence. We attribute this deformation signal to water-related  
 558 subsidence. With the exception of the subsidence signal,  
 559 little deformation is measured across the White Mountain–  
 560 Owens Valley fault system for the same reasons stated for

561 the Fish Lake–Furnace Creek fault system. The upper limit 561  
 562 here is 5 mm/yr because of the northerly orientation of the 562  
 563 fault system. Instead, most of the signal is located across the 563  
 564 Hunter Mountain (HM) fault.

#### 565 **5. Modeling the Strain Accumulation Across the 565 566 Hunter Mountain Fault**

[45] In order to analyze the signal across the Hunter 567  
 568 Mountain fault, we remove the Eureka Valley coseismic 568  
 569 displacement field. For this, we first divide the displacement 569  
 570 time series into a preearthquake and a postearthquake time 570  
 571 series. After subtracting linear trends from both time series, 571  
 572 we compute the respective mean values and obtain a pre- 572  
 573 earthquake mean position and a postearthquake mean 573  
 574 position. We then subtract the preearthquake mean position 574  
 575 from the postearthquake mean position to obtain the co- 575  
 576 seismic offset and subtract it from the displacement at each 576  
 577 postearthquake epoch. We then recalculate the velocity map. 577

[46] A profile perpendicular to the Hunter Mountain fault 578  
 (Figure 15) reveals a LOS velocity change of  $1.6 \pm 0.6$  mm/yr 579  
 across the fault. The LOS velocity change occurs progres- 580  
 sively across a zone with a width of 5–12 km centered on the 581  
 fault. Unwrapping errors or atmospheric phase residuals are 582  
 unlikely to be the cause of the observed signal as temporal 583  
 coherence masking and atmospheric phase filtering has been 584  
 applied; this leads us to consider that the signal across the 585  
 Hunter Mountain fault contains only surface deformation. 586  
 We observe that a hydrological signal affects the basin north 587  
 of the Hunter Mountain fault in some of our interferograms. 588  
 The spatial and temporal characteristics of this signal are 589  
 similar to the characteristics of atmospheric perturbations 590

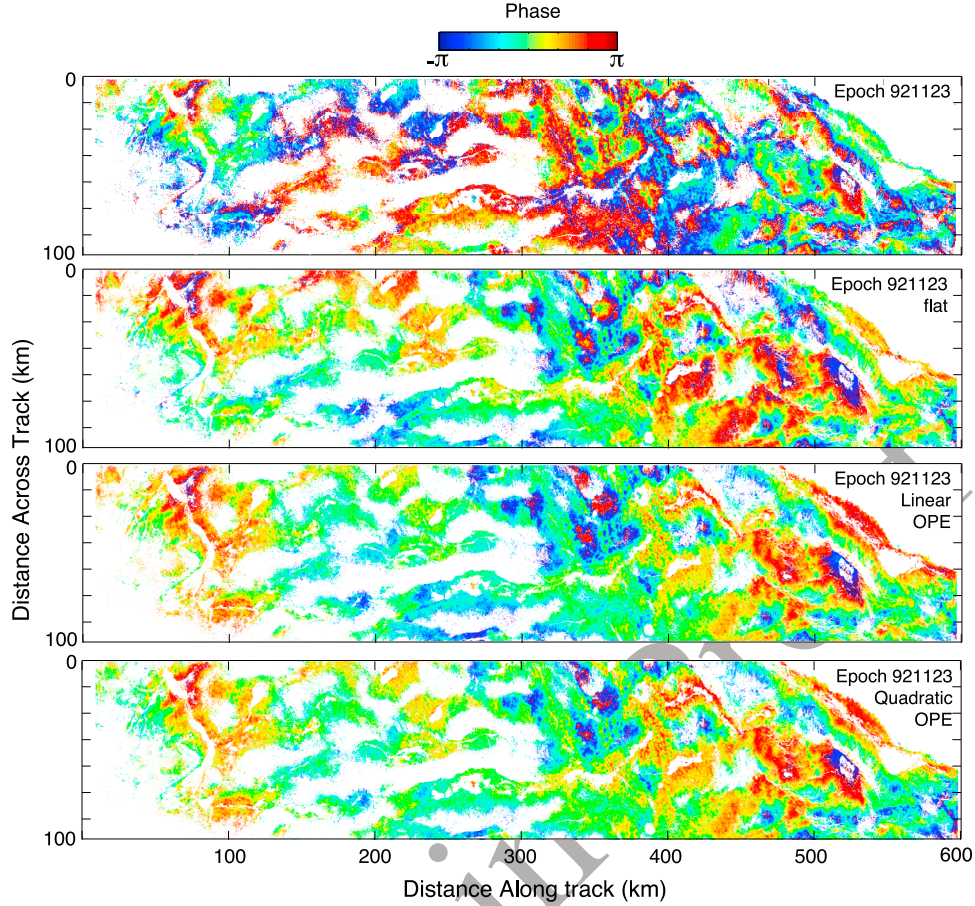


**Figure 12.** From top to bottom: Phase at 23 November 1992 epoch, phase after flattening, phase after removal of linear orbital model, phase after removal of quadratic orbital model.

591 and are removed by processing of data over a long time  
592 period and by applying spatial and temporal filtering.

593 [47] We now assume that the velocity change across the  
594 Hunter Mountain fault is the result of interseismic strain  
595 accumulation along a pure right-lateral strike-slip fault. We  
596 note that the lack of a discontinuity suggests that there is no  
597 or little surface creep. We use the classical elastic disloca-  
598 tion model of *Savage and Burford* [1973], in which the fault  
599 is driven from a freely slipping fault at depth embedded in  
600 an elastic half-space. The model has two parameters: the  
601 far-field velocity (corresponding to the slip rate of the  
602 freely slipping fault at depth) and the locking depth  
603 [*Savage and Burford*, 1973; *Weertman and Weertman*, 1964]  
604 (Figure 15). We use a nonlinear Gibbs sampling inversion  
605 scheme to retrieve the two parameters and their probability  
606 density distributions [*Johnson and Segall*, 2004]. This simple  
607 model fits the data very well. The best fit is obtained for a slip  
608 rate of  $4.9 \pm 0.8$  mm/yr and a locking depth of  $2 \pm 0.4$  km  
609 (Figure 16). Note that there is little correlation between the  
610 fault slip rate and the locking depth.

611 [48] Additional modeling of the deformation across the  
612 Hunter Mountain fault suggests that neither surface creep  
613 nor viscoelastic relaxation is occurring. A model including  
614 shallow creep [*Savage and Lisowski*, 1993] predicts no  
615 displacement on the shallow creeping section. We also  
616 tested models including viscoelastic relaxation, with model

parameters locking depth, fault slip rate, time since the last 617 earthquake, recurrence interval, and viscosity [*Savage and* 618 *Lisowski*, 1998]. The best fitting models are characterized 619 by similar values for the time since the last earthquake and 620 the recurrence time, implying that the viscoelastic relaxation 621 is completed (assuming a viscosity of  $10^{19}$  Pa s) [*Dixon et* 622 *al.*, 2003; *Thatcher and Pollitz*, 2008]. In conclusion, the 623 InSAR data are well modeled with a simple screw disloca- 624 tion in an elastic medium and do not require surface fault 625 creep or viscoelastic rheology. 626

## 6. Discussion

[49] The InSAR results across the eastern California shear 628 zone reveal a narrow zone of deformation across the Hunter 629 Mountain fault. The observations are well explained using 630 the *Savage and Burford* [1973] elastic dislocation model 631 with a vertical strike-slip fault with a 2 km locking depth 632 and a slip rate of 4.9 mm/yr. 633

[50] The OPE removal method is not essential to study the 634 deformation across the Hunter Mountain fault as the 635 wavelength of the two processes are very different. How- 636 ever, our method resolves the plane ambiguity resulting 637 from either OPE residuals or large-scale deformation due to 638 nearby faults. The OPE removal shows that the ground 639 deformation across the Hunter Mountain fault results only 640

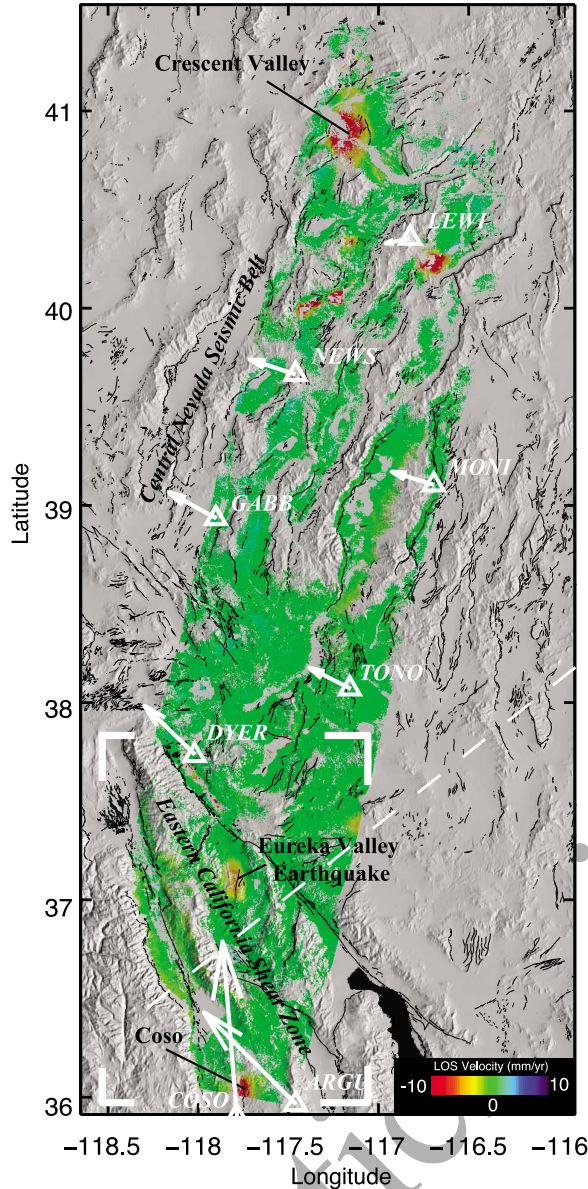


**Figure 13.** InSAR velocity map across the Basin and Range and horizontal velocity of PBO continuous GPS [Bennett et al., 2003]. Location of Figure 14 in inset. Location of profile perpendicular to ECSZ from Figure 9 between 300 and 600 km distance along profile.

641 from the Hunter Mountain fault with little effects from the  
642 Owens Valley and Death Valley fault systems.

643 [51] The slip rate of the Hunter Mountain fault estimated  
644 from the geodetic data is within the higher end of the range  
645 of geologic rates bracketed between 2.4 and 4 mm/yr  
646 [Gourmelen, 2009]. The geologic rates have been inferred  
647 from the total fault offset since fault initiation. One expla-  
648 nation for this difference in rate is that the fault has been  
649 accelerating through geologic times. Gourmelen [2009]  
650 proposed a model of fault evolution in which the slip rate  
651 increased as the fault matured and propose a model that  
652 accounts for the distribution of slip rate for different periods  
653 of activity of the Hunter Mountain fault.

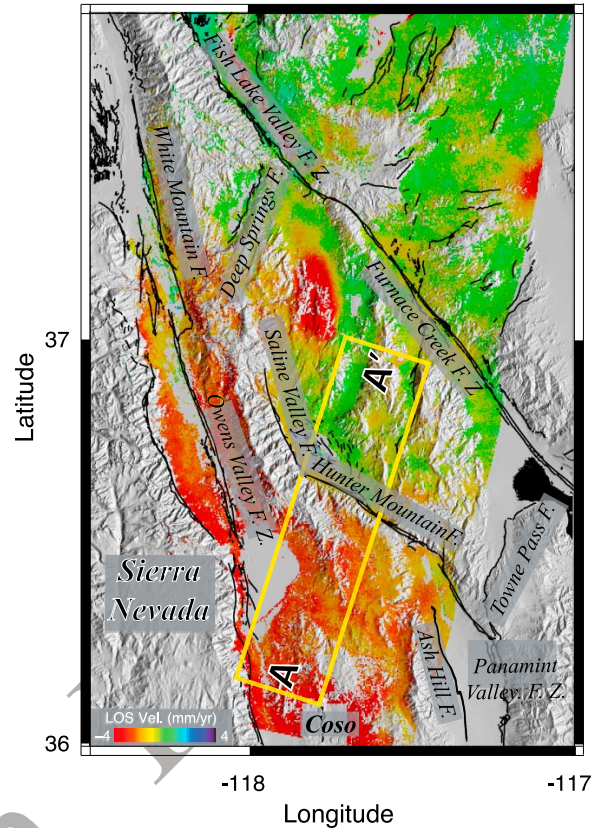


**Figure 14.** Velocity change across the eastern California shear zone. Yellow box: location of profile in Figure 15.

[52] Our locking depth estimation for the Hunter Mountain fault is significantly shallower than locking depth estimates of nearby faults which generally range between 5 and 15 km [Dixon et al., 2003; Bennett et al., 1997; Peltzer et al., 2001; McClusky et al., 2001; Gourmelen and Amelung, 2005; 654  
655  
656  
657  
658

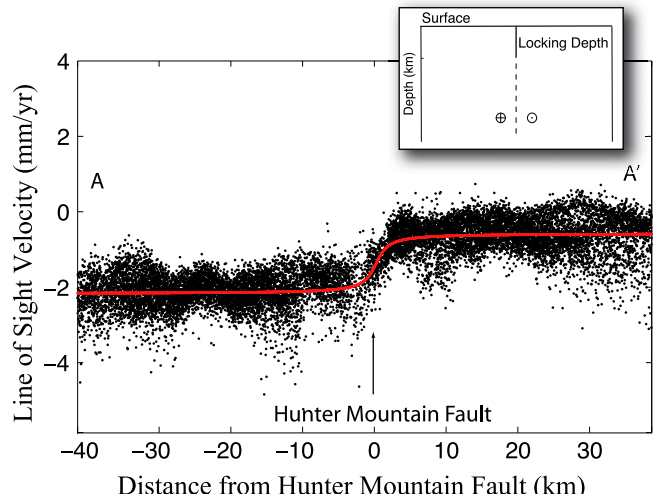


**Figure 15.** LOS velocity perpendicular to the Hunter Mountain fault. The area covered is shown in Figure 11. Fault and earth models after Savage and Burford [1973] in inset.

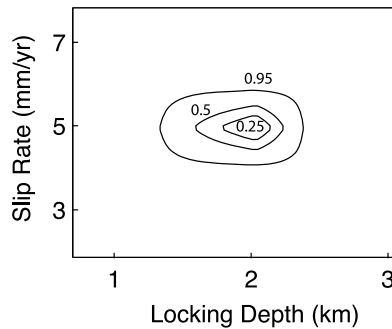


**Figure 16.** Locking depth versus slip rate probability from Gibbs sampling.

659 *Meade and Hager, 2005*. The area is characterized by shallow  
660 low seismic activity and shallow magmatism, recording  
661 between 1991 and 1995. *Feng and Lees [1998]* determine  
662 that microseismicity was localized at a depth of 3 km at the  
663 geothermal field likely related to the geothermal exploitation  
664 and at a depth of 6 km in the neighboring region. Similarly,  
665 local studies by *Walter and Weaver [1980]* and a regional  
666 study by *[Sibson 1982]* find a cutoff depth of the seismicity  
667 of 5 km, shallower than for most of California. *Wicks et al.*  
668 [2001] argue for a shallow magma body 4 km below the  
669 surface below the Coso geothermal plant. This suggests that  
670 brittle deformation occurs at shallow depth and that this  
671 depth is increasingly shallow toward the Hunter Mountain  
672 fault as shown by the shallow locking depth found in this  
673 study. These observations would support the low-angle  
674 normal fault geometry proposed by *Biehler [1987]* and  
675 *Wesnousky and Jones [1994]* (Figure 17). In this system, the  
676 Hunter Mountain fault would play the role of a transfer fault  
677 which deformation would be driven by the motion of the  
678 Panamint and Saline Valley faults. This interpretation is  
679 however speculative at this point and would benefit from a  
680 more complex modeling of the fault system and surface  
681 deformation. If the low-angle fault system was to be active,

it would have consequences on the current slip rate estimates 682  
over the ECSZ. 683

## 7. Conclusion

[53] 1. We review the theoretical framework for orbital 685  
phase errors (OPE) in InSAR time series. Orbital phase er- 686  
rors are related to uncertainties in the satellite position 687  
during image acquisitions. They impact the ability of InSAR 688  
to precisely measure subtle, long-wavelength deformation 689  
(over several hundred kilometers). 690

[54] 2. The orbital phase error at a given epoch can be 691  
expressed in terms of the horizontal and vertical baseline 692  
errors (difference in satellite position at a given epoch with 693  
respect to the first epoch) (equation (20)). The baseline errors 694  
at a given epoch are a function of along-track position. 695  
Assuming that their along-track variation can be approxi- 696  
mated by second-order polynomials, the orbital phase error 697  
is described by six parameters (equation (24)). In the absence 698  
of deformation, the orbital phase errors can be estimated 699  
directly from the InSAR data. In the presence of deformation, 700  
they can be estimated using independent information such as 701  
from models or GPS (equation (25)). 702

[55] 3. We apply this method to the eastern California 703  
shear zone using 44 ERS SAR acquisitions from 1992 to 2001 704  
and data from six continuous GPS stations starting in 1999. 705  
Using this method, InSAR recovers the long-wavelength 706  
deformation of the region known from GPS (Figure 9). 707

[56] 4. The corrected InSAR time series data reveal a 708  
region of rapid velocity change across the Hunter Mountain 709  
fault. Observed ground deformation is interpreted as caused 710  
by interseismic strain accumulation across a strike-slip fault. 711  
Modeling with the classical *Savage and Burford [1973]* 712  
elastic model suggests a locking depth of  $2 \pm 0.4$  km and 713  
a slip rate of  $4.9 \pm 0.8$  mm/yr. There is no evidence for 714  
surface creep. 715

[57] 5. The geodetic slip rate of the Hunter Mountain fault 716  
is faster than geologic slip rates, suggesting that the fault has 717  
accelerated over time. The locking depth is very shallow in 718  
comparison with nearby faults. This may indicate the fault 719

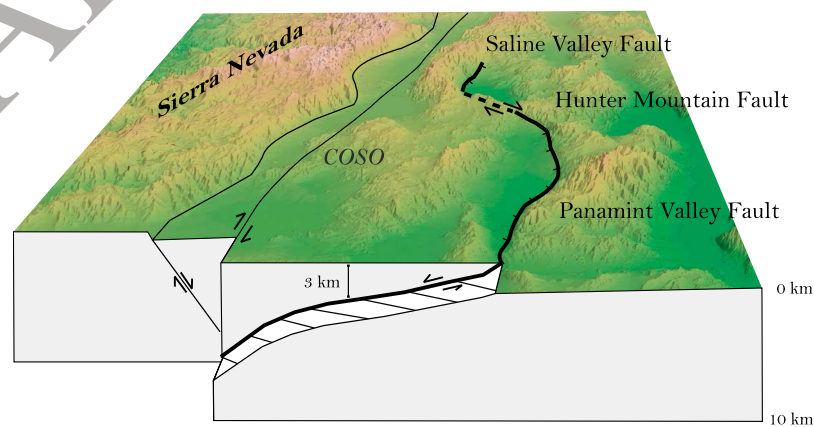


**Figure 17.** Model of present-day tectonic for the Owens Valley–Panamint Valley–Hunter Mountain–Saline Valley faults modified from *Wesnousky and Jones [1994]*. At the location of the InSAR profile, the depth of the Panamint fault is of the order of the locking depth for the Hunter Mountain fault.

720 plays a pivotal mechanical role in low angle normal fault  
721 system in the area.

722 [58] **Acknowledgments.** We thank Timothy Dixon and Freek Van  
723 Leijen for discussion and two anonymous reviewers for comments that sig-  
724 nificantly improved the manuscript. We thank Mariarosaria Manzo for her  
725 support to the SBAS-DInSAR results handling. We thank the European  
726 Space Agency for the SAR data, which were obtained through the  
727 GeoEarthscope and WinSAR projects at UNAVCO. NASA supported this  
728 research through an Earth System Science fellowship to N.G. and the  
729 National Science Foundation through grant NSF-EAR 0454552 to F.A.

## 730 References

- 731 Amelung, F., S. Jonsson, H. Zebker, and P. Segall (2000), Widespread  
732 uplift and “trapdoor” faulting on Galapagos volcanoes observed with  
733 radar interferometry, *Nature*, **407**, 993–996.
- 734 Bennett, R. A., B. P. Wernicke, J. L. Davis, P. Elosegui, J. K. Snow, M. J.  
735 Abolins, M. A. House, G. L. Stirewalt, and D. A. Ferrill (1997), Global  
736 positioning system constraints on fault slip rates in the Death Valley  
737 region, California and Nevada, *Geophys. Res. Lett.*, **24**, 3073–3076,  
738 doi:10.1029/97GL02951.
- 739 Bennett, R. A., B. P. Wernicke, N. A. Niemi, A. M. Friedrich, and J. L.  
740 Davis (2003), Contemporary strain rates in the northern Basin and Range  
741 province from GPS data, *Tectonics*, **22**(2), 1008, doi:10.1029/  
742 2001TC001355.
- 743 Berardino, P., G. Fornaro, R. Lanari, and E. Sansosti (2002), A new algo-  
744 rithm for surface deformation monitoring based on small baseline differ-  
745 ential SAR interferograms, *IEEE Trans. Geosci. Remote Sens.*, **40**(11),  
746 2375–2383.
- 747 Biehler, S. (1987), A geophysical investigation of the Northern Panamint  
748 Valley, Inyo County, California: Evidence for possible low-angle normal  
749 faulting at shallow depth in the crust, *J. Geophys. Res.*, **92**, 10427–10441,  
750 doi:10.1029/JB092iB10p10427.
- 751 Biggs, J., T. Wright, Z. Lu, and B. Parsons (2007), Multi-interferogram  
752 method for measuring interseismic deformation: Denali fault, Alaska,  
753 *Geophys. J. Int.*, **170**, 1165–1179.
- 754 Burchfiel, B. C., K. V. Hodges, and L. H. Royden (1987), Geology of Panamint  
755 Valley–Saline Valley pull-apart system, California–Palinspastic evi-  
756 dence for low-angle geometry of a Neogene range-bounding fault,  
757 *J. Geophys. Res.*, **92**, 10422–10426, doi:10.1029/JB092iB10p10422.
- 758 Burgmann, R., G. Hillesy, A. Ferretti, and F. Novali (2006), Resolving ver-  
759 tical tectonics in the San Francisco Bay Area from permanent scatterer  
760 InSAR and GPS analysis, *Geology*, **34**, 221–224.
- 761 Casu, F., M. Manzo, A. Pepe, and R. Lanari (2008), SBAS-DInSAR anal-  
762 ysis of very extended areas: First results on a 60,000-km<sup>2</sup> test site, *IEEE*  
763 *Geosci. Remote Sens. Lett.*, **5**, 438–442.
- 764 Davis, J. L., B. P. Wernicke, S. Bisnath, N. A. Niemi, and P. Elosegui  
765 (2006), Subcontinental-scale crustal velocity changes along the Pacific–  
766 North American plate boundary, *Nature*, **441**, 1131–1134.
- 767 Dixon, T., F. Farina, C. DeMets, F. Suarez-Vidal, J. Fletcher, B. Marquez-  
768 Azua, M. Miller, O. Sanchez, and P. Umhoefer (2000a), New kinematic  
769 models for Pacific–North American motion from 3 Ma to present: II.  
770 Evidence for a “Baja California shear zone,” *Geophys. Res. Lett.*, **27**,  
771 3961–3964, doi:10.1029/2000GL008529.
- 772 Dixon, T. H., M. Miller, F. Farina, H. Z. Wang, and D. Johnson (2000b),  
773 Present-day motion of the Sierra Nevada block and some tectonic impli-  
774 cations for the Basin and Range province, North American Cordillera,  
775 *Tectonics*, **19**, 1–24, doi:10.1029/1998TC001088.
- 776 Dixon, T. H., E. Norabuena, and L. Hotaling (2003), Paleoseismology and  
777 Global Positioning System: Earthquake-cycle effects and geodetic versus  
778 geologic fault slip rates in the eastern California shear zone, *Geology*,  
779 **31**(1), 55–58.
- 780 Dokka, R. K., and C. J. Travis (1990a), Late Cenozoic strike-slip faulting  
781 in the Mojave Desert, California, *Tectonics*, **9**, 311–340, doi:10.1029/  
782 TC009i002p00311.
- 783 Dokka, R. K., and C. J. Travis (1990b), Role of the eastern California shear  
784 zone in accommodating Pacific–North American plate motion, *Geophys.*  
785 *Res. Lett.*, **17**, 1323–1326, doi:10.1029/GL017i009p01323.
- 786 Feng, Q., and J. M. Lees (1998), Microseismicity, stress, and fracture in the  
787 Coso geothermal field, California, *Tectonophysics*, **289**, 221–238.
- 788 Ferretti, A., C. Prati, and F. Rocca (2001), Permanent scatterers in SAR  
789 interferometry, *IEEE Trans. Geosci. Remote Sens.*, **39**, 8–20.
- 790 Ferretti, A., M. Bianchi, C. Prati, and F. Rocca (2005), Higher-order per-  
791 manent scatterers analysis, *EURASIP JASP*, **2005**, 3231–3242.
- 792 Fialko, Y. (2006), Interseismic strain accumulation and the earthquake  
793 potential on the southern San Andreas fault system, *Nature*, **441**, 968–971.
- 794 Fialko, Y., and M. Simons (2000), Deformation and seismicity in the Coso  
795 geothermal area, Inyo County, California: Observations and modeling  
796 using satellite radar interferometry, *J. Geophys. Res.*, **105**, 21781–21793,  
797 doi:10.1029/2000JB900169.
- 798 Gabriel, A. K., R. M. Goldstein, and H. A. Zebker (1989), Mapping small  
799 elevation changes over large areas – Differential radar interferometry,  
799 *J. Geophys. Res.*, **94**, 9183–9191, doi:10.1029/JB094iB07p09183.
- 800 Goldstein, R. M., H. Engelhardt, B. Kamb, and R. M. Frolich (1993), Sat-  
801 ellite radar interferometry for monitoring ice-sheet motion – Application  
802 to an Antarctic ice stream, *Science*, **262**, 1525–1530.
- 803 Gourmelen, N. (2009), Measuring low fault strain rate with synthetic aper-  
804 ture radar interferometry: Application to the Pacific–North American  
805 plate boundary., PhD thesis, Univ. of Miami, Miami.
- 806 Gourmelen, N., and F. Amelung (2005), Postseismic mantle relaxation in  
807 the Central Nevada Seismic Belt, *Science*, **310**, 1473–1476.
- 808 Gourmelen, N., F. Amelung, F. Casu, M. Manzo, and R. Lanari (2007),  
809 Mining-related ground deformation in Crescent Valley, Nevada: Implica-  
810 tions for sparse GPS networks, *Geophys. Res. Lett.*, **34**, L09309,  
811 doi:10.1029/2007GL029427.
- 812 Hanssen, R. (2001), *Radar Interferometry – Data Interpretation and Error  
Analysis*, Kluwer Academic Publishers, Dordrecht.
- 813 Hodges, K. V., L. W. McKenna, J. Stock, J. Knapp, L. Page, K. Sternlof,  
814 D. Silverberg, G. Wust, and J. D. Walker (1989), Evolution of exten-  
815 sional basins and Basin and Range topography west of Death Valley,  
816 California, *Tectonics*, **8**(3), 453–467, doi:10.1029/TC008i003p00453.
- 817 Hooper, A., H. Zebker, P. Segall, and B. Kampes (2004), A new method  
818 for measuring deformation on volcanoes and other natural terrains using  
819 InSAR persistent scatterers, *Geophys. Res. Lett.*, **31**, L23611,  
820 doi:10.1029/2004GL021737.
- 821 Johnson, K. M., and P. Segall (2004), Viscoelastic earthquake cycle models  
822 with deep stress-driven creep along the San Andreas fault system,  
823 *J. Geophys. Res.*, **109**, B10403, doi:10.1029/2004JB003096.
- 824 Kohlhase, A. O., K. L. Feigl, and D. Massonnet (2003), Applying differ-  
825 ential InSAR to orbital dynamics: a new approach for estimating ERS tra-  
826 jectories, *J. Geodesy*, **77**(9), 493–502.
- 827 Kreemer, C., G. Blewitt, and W. C. Hammond (2006), Using geodesy to  
828 explore correlations between crustal deformation characteristics and geo-  
829 thermal resources, p. 20, Geothermal Resources Council Annual Meeting,  
830 San Diego.
- 831 Lanari, R., O. Mora, M. Manunta, J. J. Mallorqui, P. Berardino, and E. San-  
832 sosti (2004), A small-baseline approach for investigating deformations  
833 on full-resolution differential SAR interferograms, *IEEE Trans. Geosci.  
834 Remote Sens.*, **42**, 1377–1386.
- 835 Lanari, R., F. Casu, M. Manzo, G. Zeni, P. Berardino, M. Manunta, and  
836 A. Pepe (2007), An overview of the small baseline subset algorithm: A  
837 DInSAR technique for surface deformation analysis, *Pure Appl. Geo-  
838 phys.*, **164**, 637–661.
- 839 Lee, J., D. F. Stockli, L. A. Owen, R. C. Finkel, and R. Kisiltsyn (2009),  
840 Exhumation of the Inyo Mountains, California: Implications for the timing  
841 of extension along the western boundary of the Basin and Range Province  
842 and distribution of dextral fault slip rates across the eastern California shear  
843 zone, *Tectonics*, **28**, TC1001, doi:10.1029/2008TC002295.
- 844 Massonnet, D. (1997), Satellite radar interferometry, *Sci. Am.*, **276**, 46–53.
- 845 Massonnet, D., and K. L. Feigl (1998), Radar interferometry and its appli-  
846 cation to changes in the earth’s surface, *Rev. Geophys.*, **36**, 441–500,  
847 doi:10.1029/97RG03139.
- 848 Massonnet, D., K. Feigl, M. Rossi, and F. Adragna (1994), Radar interfer-  
849 metric mapping of deformation in the year after the Landers earthquake,  
850 *Nature*, **369**, 227–230.
- 851 McClusky, S. C., S. C. Bjornstad, B. H. Hager, R. W. King, B. J. Meade,  
852 M. M. Miller, F. C. Monastero, and B. J. Souter (2001), Present day kine-  
853 matics of the eastern California shear zone from a geodetically con-  
854 strained block model, *Geophys. Res. Lett.*, **28**, 3369–3372,  
855 doi:10.1029/2000GL011851.
- 856 Meade, B. J., and B. H. Hager (2005), Block models of crustal motion in  
857 southern California constrained by GPS measurements, *J. Geophys.  
858 Res.*, **110**, B03403, doi:10.1029/2004JB003209.
- 859 Oswald, J. A., and S. G. Wesnousky (2002), Neotectonics and quaternary  
860 geology of the Hunter Mountain fault zone and Saline Valley region,  
861 southeastern California, *Geomorphology*, **42**(3), 255–278.
- 862 Peltzer, G., and P. Rosen (1995), Surface displacements of the 17 May  
863 1993 Eureka Valley, California, earthquake observed by SAR interferom-  
864 etry, *Science*, **268**, 1333–1336.
- 865 Peltzer, G., F. Crampé, S. Hensley, and P. Rosen (2001), Transient strain  
866 accumulation and fault interaction in the eastern California shear zone,  
867 *Geology*, **29**, 975–978.
- 868 Pepe, A., and R. Lanari (2006), On the extension of the minimum cost flow  
869 algorithm for phase unwrapping of multitemporal differential SAR inter-  
870 ferograms, *IEEE Trans. Geosci. Remote Sens.*, **44**, 2374–2383.
- 871 Fialko, Y., and M. Simons (2000), Deformation and seismicity in the Coso  
872 geothermal area, Inyo County, California: Observations and modeling  
873 using satellite radar interferometry, *J. Geophys. Res.*, **105**, 21781–21793,  
874 doi:10.1029/2000JB900169.
- 875 Fialko, Y., and M. Simons (2000), Deformation and seismicity in the Coso  
876 geothermal area, Inyo County, California: Observations and modeling  
877 using satellite radar interferometry, *J. Geophys. Res.*, **105**, 21781–21793,  
878 doi:10.1029/2000JB900169.
- 879 Fialko, Y., and M. Simons (2000), Deformation and seismicity in the Coso  
880 geothermal area, Inyo County, California: Observations and modeling  
881 using satellite radar interferometry, *J. Geophys. Res.*, **105**, 21781–21793,  
882 doi:10.1029/2000JB900169.
- 883 Fialko, Y., and M. Simons (2000), Deformation and seismicity in the Coso  
884 geothermal area, Inyo County, California: Observations and modeling  
885 using satellite radar interferometry, *J. Geophys. Res.*, **105**, 21781–21793,  
886 doi:10.1029/2000JB900169.
- 887 Fialko, Y., and M. Simons (2000), Deformation and seismicity in the Coso  
888 geothermal area, Inyo County, California: Observations and modeling  
889 using satellite radar interferometry, *J. Geophys. Res.*, **105**, 21781–21793,  
890 doi:10.1029/2000JB900169.
- 891 Fialko, Y., and M. Simons (2000), Deformation and seismicity in the Coso  
892 geothermal area, Inyo County, California: Observations and modeling  
893 using satellite radar interferometry, *J. Geophys. Res.*, **105**, 21781–21793,  
894 doi:10.1029/2000JB900169.
- 895 Fialko, Y., and M. Simons (2000), Deformation and seismicity in the Coso  
896 geothermal area, Inyo County, California: Observations and modeling  
897 using satellite radar interferometry, *J. Geophys. Res.*, **105**, 21781–21793,  
898 doi:10.1029/2000JB900169.
- 899 Fialko, Y., and M. Simons (2000), Deformation and seismicity in the Coso  
900 geothermal area, Inyo County, California: Observations and modeling  
901 using satellite radar interferometry, *J. Geophys. Res.*, **105**, 21781–21793,  
902 doi:10.1029/2000JB900169.
- 903 Fialko, Y., and M. Simons (2000), Deformation and seismicity in the Coso  
904 geothermal area, Inyo County, California: Observations and modeling  
905 using satellite radar interferometry, *J. Geophys. Res.*, **105**, 21781–21793,  
906 doi:10.1029/2000JB900169.
- 907 Fialko, Y., and M. Simons (2000), Deformation and seismicity in the Coso  
908 geothermal area, Inyo County, California: Observations and modeling  
909 using satellite radar interferometry, *J. Geophys. Res.*, **105**, 21781–21793,  
910 doi:10.1029/2000JB900169.
- 911 Fialko, Y., and M. Simons (2000), Deformation and seismicity in the Coso  
912 geothermal area, Inyo County, California: Observations and modeling  
913 using satellite radar interferometry, *J. Geophys. Res.*, **105**, 21781–21793,  
914 doi:10.1029/2000JB900169.
- 915 Fialko, Y., and M. Simons (2000), Deformation and seismicity in the Coso  
916 geothermal area, Inyo County, California: Observations and modeling  
917 using satellite radar interferometry, *J. Geophys. Res.*, **105**, 21781–21793,  
918 doi:10.1029/2000JB900169.
- 919 Fialko, Y., and M. Simons (2000), Deformation and seismicity in the Coso  
920 geothermal area, Inyo County, California: Observations and modeling  
921 using satellite radar interferometry, *J. Geophys. Res.*, **105**, 21781–21793,  
922 doi:10.1029/2000JB900169.
- 923 Fialko, Y., and M. Simons (2000), Deformation and seismicity in the Coso  
924 geothermal area, Inyo County, California: Observations and modeling  
925 using satellite radar interferometry, *J. Geophys. Res.*, **105**, 21781–21793,  
926 doi:10.1029/2000JB900169.
- 927 Fialko, Y., and M. Simons (2000), Deformation and seismicity in the Coso  
928 geothermal area, Inyo County, California: Observations and modeling  
929 using satellite radar interferometry, *J. Geophys. Res.*, **105**, 21781–21793,  
930 doi:10.1029/2000JB900169.
- 931 Fialko, Y., and M. Simons (2000), Deformation and seismicity in the Coso  
932 geothermal area, Inyo County, California: Observations and modeling  
933 using satellite radar interferometry, *J. Geophys. Res.*, **105**, 21781–21793,  
934 doi:10.1029/2000JB900169.
- 935 Fialko, Y., and M. Simons (2000), Deformation and seismicity in the Coso  
936 geothermal area, Inyo County, California: Observations and modeling  
937 using satellite radar interferometry, *J. Geophys. Res.*, **105**, 21781–21793,  
938 doi:10.1029/2000JB900169.
- 939 Fialko, Y., and M. Simons (2000), Deformation and seismicity in the Coso  
940 geothermal area, Inyo County, California: Observations and modeling  
941 using satellite radar interferometry, *J. Geophys. Res.*, **105**, 21781–21793,  
942 doi:10.1029/2000JB900169.
- 943 Fialko, Y., and M. Simons (2000), Deformation and seismicity in the Coso  
944 geothermal area, Inyo County, California: Observations and modeling  
945 using satellite radar interferometry, *J. Geophys. Res.*, **105**, 21781–21793,  
946 doi:10.1029/2000JB900169.
- 947 Fialko, Y., and M. Simons (2000), Deformation and seismicity in the Coso  
948 geothermal area, Inyo County, California: Observations and modeling  
949 using satellite radar interferometry, *J. Geophys. Res.*, **105**, 21781–21793,  
950 doi:10.1029/2000JB900169.
- 951 Fialko, Y., and M. Simons (2000), Deformation and seismicity in the Coso  
952 geothermal area, Inyo County, California: Observations and modeling  
953 using satellite radar interferometry, *J. Geophys. Res.*, **105**, 21781–21793,  
954 doi:10.1029/2000JB900169.
- 955 Fialko, Y., and M. Simons (2000), Deformation and seismicity in the Coso  
956 geothermal area, Inyo County, California: Observations and modeling  
957 using satellite radar interferometry, *J. Geophys. Res.*, **105**, 21781–21793,  
958 doi:10.1029/2000JB900169.
- 959 Fialko, Y., and M. Simons (2000), Deformation and seismicity in the Coso  
960 geothermal area, Inyo County, California: Observations and modeling  
961 using satellite radar interferometry, *J. Geophys. Res.*, **105**, 21781–21793,  
962 doi:10.1029/2000JB900169.
- 963 Fialko, Y., and M. Simons (2000), Deformation and seismicity in the Coso  
964 geothermal area, Inyo County, California: Observations and modeling  
965 using satellite radar interferometry, *J. Geophys. Res.*, **105**, 21781–21793,  
966 doi:10.1029/2000JB900169.
- 967 Fialko, Y., and M. Simons (2000), Deformation and seismicity in the Coso  
968 geothermal area, Inyo County, California: Observations and modeling  
969 using satellite radar interferometry, *J. Geophys. Res.*, **105**, 21781–21793,  
970 doi:10.1029/2000JB900169.
- 971 Fialko, Y., and M. Simons (2000), Deformation and seismicity in the Coso  
972 geothermal area, Inyo County, California: Observations and modeling  
973 using satellite radar interferometry, *J. Geophys. Res.*, **105**, 21781–21793,  
974 doi:10.1029/2000JB900169.
- 975 Fialko, Y., and M. Simons (2000), Deformation and seismicity in the Coso  
976 geothermal area, Inyo County, California: Observations and modeling  
977 using satellite radar interferometry, *J. Geophys. Res.*, **105**, 21781–21793,  
978 doi:10.1029/2000JB900169.
- 979 Fialko, Y., and M. Simons (2000), Deformation and seismicity in the Coso  
980 geothermal area, Inyo County, California: Observations and modeling  
981 using satellite radar interferometry, *J. Geophys. Res.*, **105**, 21781–21793,  
982 doi:10.1029/2000JB900169.
- 983 Fialko, Y., and M. Simons (2000), Deformation and seismicity in the Coso  
984 geothermal area, Inyo County, California: Observations and modeling  
985 using satellite radar interferometry, *J. Geophys. Res.*, **105**, 21781–21793,  
986 doi:10.1029/2000JB900169.
- 987 Fialko, Y., and M. Simons (2000), Deformation and seismicity in the Coso  
988 geothermal area, Inyo County, California: Observations and modeling  
989 using satellite radar interferometry, *J. Geophys. Res.*, **105**, 21781–21793,  
990 doi:10.1029/2000JB900169.
- 991 Fialko, Y., and M. Simons (2000), Deformation and seismicity in the Coso  
992 geothermal area, Inyo County, California: Observations and modeling  
993 using satellite radar interferometry, *J. Geophys. Res.*, **105**, 21781–21793,  
994 doi:10.1029/2000JB900169.
- 995 Fialko, Y., and M. Simons (2000), Deformation and seismicity in the Coso  
996 geothermal area, Inyo County, California: Observations and modeling  
997 using satellite radar interferometry, *J. Geophys. Res.*, **105**, 21781–21793,  
998 doi:10.1029/2000JB900169.
- 999 Fialko, Y., and M. Simons (2000), Deformation and seismicity in the Coso  
1000 geothermal area, Inyo County, California: Observations and modeling  
1001 using satellite radar interferometry, *J. Geophys. Res.*, **105**, 21781–21793,  
1002 doi:10.1029/2000JB900169.

- 873 Pollitz, F. F., G. Peltzer, and R. Burgmann (2000), Mobility of continental  
 874 mantle: Evidence from postseismic geodetic observations following the  
 875 1992 Landers earthquake, *J. Geophys. Res.*, **105**, 8035–8054,  
 876 doi:10.1029/1999JB900380.
- 877 Rosen, P. A., S. Hensley, I. R. Joughin, F. K. Li, S. N. Madsen, E. Rodriguez,  
 878 and R. M. Goldstein (2000), Synthetic aperture radar interferometry -  
 879 Invited paper, *Proc. IEEE*, **88**, 333–382.
- 880 Rosen, P. A., S. Henley, G. Peltzer, and M. Simons (2004), Updated repeat  
 881 orbit interferometry package released, *Eos Trans. AGU*, **85**.
- 882 Savage, J. C., and M. Lisowski (1993), Inferred depth of creep on the Hay-  
 883 ward fault, Central California, *J. Geophys. Res.*, **98**, 787–793, doi:10.1029/  
 884 92JB01871.
- 885 Savage, J. C., and M. Lisowski (1998), Viscoelastic coupling model of the  
 886 San Andreas fault along the big bend, southern California, *J. Geophys.  
 887 Res.*, **103**, 7281–7292, doi:10.1029/98JB00148.
- 888 Savage, J. C., and R. O. Burford (1973), Geodetic determination of relative  
 889 plate motion in Central California, *J. Geophys. Res.*, **78**, 832–845,  
 890 doi:10.1029/JB078i005p00832.
- 891 Scharroo, R. (2002), A Decade of ERS Satellite Orbits and Altimetry, Delft  
 892 Univ. Technology, Netherlands.
- 893 Schmalzle, G. (2008), The Earthquake Cycle of Strike-Slip Faults, PhD  
 894 thesis, Univ. of Miami, Miami.
- 895 Sibson, R. H. (1982), Fault zone models, heat-flow, and the depth distribu-  
 896 tion of earthquakes in the continental-crust of the United-States, *Bull.  
 897 Seismol. Soc. Am.*, **72**, 151–163.
- 898 Sternloff, K. R. (1988), Structural Style and Kinematic History of the  
 899 Active Panamint-Saline Extensional System, 30 pp., MIT., Inyo County,  
 900 California.
- 901 Thatcher, W., and F. F. Pollitz (2008), Temporal evolution of continental  
 902 lithospheric strength in actively deforming regions, *GSA Today*, **18**, 4–11.
- Walter, A. W., and C. S. Weaver (1980), Seismicity of the Coso Range, 903  
 California, *J. Geophys. Res.*, **85**, 2441–2458, doi:10.1029/  
 JB085iB05p02441.
- Weertman, J., and J. R. Weertman (1964), *Elementary Dislocation Theory*, 906  
 213 pp., Macmillan, New York.
- Wernicke, B., A. M. Friedrich, N. A. Niemi, R. A. Bennett, and J. L. Davis 908  
 (2000), Dynamics of plate boundary fault systems from Basin and Range  
 Geodetic Network (BARGEN) and geological data, *GSA Today*, **10**, 1–7.
- Wesnousky, S. G., and C. H. Jones (1994), Oblique slip, slip partitioning, 911  
 spatial and temporal changes in the regional stress-field, and the relative  
 912 strength of active faults in the Basin and Range, Western United States,  
 913 *Geology*, **22**, 1031–1034.
- Wicks, C. W., W. Thatcher, F. C. Monastero, and M. A. Hasting (2001), 915  
 Steady state deformation of the Coso Range, east central California,  
 inferred from satellite radar interferometry, *J. Geophys. Res.*, **106**, 916  
 13769–13780, doi:10.1029/2001JB000298.
- Wright, T. J., B. Parsons, P. C. England, and E. J. Fielding (2004), InSAR 919  
 observations of low slip rates on the major faults of western Tibet, *Science*, 920  
**305**, 236–239.
- Zhang, P. Z., M. Ellis, D. B. Slemmons, and F. Y. Mao (1990), Right-lateral 922  
 displacements and the holocene slip rate associated with prehistoric earth- 923  
 quakes along the southern Panamint Valley fault zone: Implications for 924  
 southern Basin and Range tectonics and coastal California deformation, 925  
*J. Geophys. Res.*, **95**, 4857–4872, doi:10.1029/JB095iB04p04857.
- F. Amelung, School of Marine and Atmospheric Science, University of 927  
 Miami, Miami, FL, USA. 928
- N. Gourmelen, School of Earth and Environment, University of Leeds, 929  
 Leeds, UK. (n.gourmelen@leeds.ac.uk) 930
- R. Lanari, IREA, Napoli, Italy. 931